

## INFORMATION TO USERS

This material was produced from a microfilm copy of the original document. While the most advanced technological means to photograph and reproduce this document have been used, the quality is heavily dependent upon the quality of the original submitted.

The following explanation of techniques is provided to help you understand markings or patterns which may appear on this reproduction.

1. The sign or "target" for pages apparently lacking from the document photographed is "Missing Page(s)". If it was possible to obtain the missing page(s) or section, they are spliced into the film along with adjacent pages. This may have necessitated cutting thru an image and duplicating adjacent pages to insure you complete continuity.
2. When an image on the film is obliterated with a large round black mark, it is an indication that the photographer suspected that the copy may have moved during exposure and thus cause a blurred image. You will find a good image of the page in the adjacent frame.
3. When a map, drawing or chart, etc., was part of the material being photographed the photographer followed a definite method in "sectioning" the material. It is customary to begin photoing at the upper left hand corner of a large sheet and to continue photoing from left to right in equal sections with a small overlap. If necessary, sectioning is continued again – beginning below the first row and continuing on until complete.
4. The majority of users indicate that the textual content is of greatest value, however, a somewhat higher quality reproduction could be made from "photographs" if essential to the understanding of the dissertation. Silver prints of "photographs" may be ordered at additional charge by writing the Order Department, giving the catalog number, title, author and specific pages you wish reproduced.
5. PLEASE NOTE: Some pages may have indistinct print. Filmed as received.

**Xerox University Microfilms**

300 North Zeeb Road  
Ann Arbor, Michigan 48106

75-26,930

BALDA, Raymond Joseph, 1942-  
A SILICON JUNCTION SOLAR ENERGY CONVERTER.

The University of Arizona, Ph.D., 1975  
Engineering, electronics and electrical

**Xerox University Microfilms**, Ann Arbor, Michigan 48106

© COPYRIGHTED

BY

RAYMOND JOSEPH BALDA

1975

iii

**THIS DISSERTATION HAS BEEN MICROFILMED EXACTLY AS RECEIVED.**

A SILICON JUNCTION SOLAR ENERGY CONVERTER

by

Raymond Joseph Balda

---

A Dissertation Submitted to the Faculty of the

DEPARTMENT OF ELECTRICAL ENGINEERING

In Partial Fulfillment of the Requirements  
For the Degree of

DOCTOR OF PHILOSOPHY

In the Graduate College

THE UNIVERSITY OF ARIZONA

1 9 7 5

THE UNIVERSITY OF ARIZONA

GRADUATE COLLEGE

I hereby recommend that this dissertation prepared under my  
direction by Raymond Joseph Balda

entitled A Silicon Junction Solar Energy Converter

be accepted as fulfilling the dissertation requirement of the  
degree of Doctor of Philosophy

John A. Reagan April 30, 1975  
Dissertation Director Date

After inspection of the final copy of the dissertation, the  
following members of the Final Examination Committee concur in  
its approval and recommend its acceptance:\*

<u>John O. Kuc</u>	<u>April 30/75</u>
<u>Reginald L. Call</u>	<u>30 Apr - 1975</u>
<u>D. Hamilton</u>	<u>Apr 30, 1975</u>
<u>R. H. Chambers</u>	<u>May, 1, 1975</u>

\*This approval and acceptance is contingent on the candidate's  
adequate performance and defense of this dissertation at the  
final oral examination. The inclusion of this sheet bound into  
the library copy of the dissertation is evidence of satisfactory  
performance at the final examination.

STATEMENT BY AUTHOR

This dissertation has been submitted in partial fulfillment of requirements for an advanced degree at The University of Arizona and is deposited in the University Library to be made available to borrowers under rules of the Library.

Brief quotations from this dissertation are allowable without special permission, provided that accurate acknowledgment of source is made. Requests for permission for extended quotation from or reproduction of this manuscript in whole or in part may be granted by the copyright holder.

SIGNED: Raymond J Balda

## ACKNOWLEDGMENTS

It is a pleasure for the author to take this opportunity to express his sincere gratitude to his dissertation director, Dr. John A. Reagan, for the continued encouragement, guidance, patience, and support offered by him through the duration of this study. The author also acknowledges the many helpful suggestions given by Dr. Donald G. Dudley concerning the mathematical modeling and also by Dr. Victor A. Wells and Dr. William J. Lillis concerning silicon device processing.

The author wishes to extend his deep appreciation to his wife, Joan, for her support, continued encouragement and sacrifices during the course of his graduate program.

This work was partially supported by the National Aeronautics and Space Administration, Contract NAS2-5883.

TABLE OF CONTENTS

		Page
	LIST OF ILLUSTRATIONS . . . . .	vi
	LIST OF TABLES . . . . .	vii
	ABSTRACT . . . . .	viii
CHAPTER		
1	INTRODUCTION . . . . .	1
2	DEVICE FABRICATION AND TEST . . . . .	9
	Fabrication . . . . .	9
	Test . . . . .	20
3	THEORETICAL ANALYSIS . . . . .	25
4	RESULTS . . . . .	46
	Experimental Results . . . . .	46
	Lot 1, Cell No. 4-E2 Large Grooves . . . . .	47
	Lot 1, Cell No. 1-A2 Small Grooves . . . . .	50
	Lot 2, Cell No. 2-B2 Small Grooves . . . . .	50
	Discussion of Test Results . . . . .	55
	Analytical Results . . . . .	58
5	CONCLUSIONS . . . . .	71
	LIST OF REFERENCES . . . . .	75

## LIST OF ILLUSTRATIONS

Figure	Page
1.1 PIN Solar Cell Profile . . . . .	4
1.2 PIN Diode of Kim and Schwartz [1969] . . . . .	7
2.1 Mask Set . . . . .	11
2.2 Effect of Mask Alignment to $\langle 111 \rangle$ Planes on Groove Dimensions . . . . .	14
2.3 Groove Profile Before and After HF:HNO <sub>3</sub> :HAc Etch . . . . .	14
2.4 Separation of Resist at the Corners of the Groove . . . . .	16
2.5 Resist Build-up Due to Multiple Application . . . . .	16
2.6 Result of Mask Misalignment on Polymerization of Resist . . . . .	18
2.7 PIN Solar Cell Test Set . . . . .	21
3.1 Geometry and Coordinate System Used in Analysis . . . . .	28
4.1 V <sub>oc</sub> Versus Cell Thickness, Cell #4-E2 . . . . .	48
4.2 I <sub>sc</sub> Versus Cell Thickness, Cell #4-E2 . . . . .	49
4.3 V <sub>oc</sub> Versus Cell Thickness, Cell #1-A2 . . . . .	51
4.4 I <sub>sc</sub> Versus Cell Thickness, Cell #1-A2 . . . . .	52
4.5 V-I Characteristic of Cell #1-A2 . . . . .	53
4.6 V-I Characteristic of Cell #2-B2 . . . . .	56
4.7 V <sub>oc</sub> Versus L*/B . . . . .	61
4.8 I <sub>sc</sub> Versus L*/B . . . . .	61
4.9 Current Versus Voltage Characteristic from Computer Analysis . . . . .	67

## LIST OF TABLES

Table		Page
4.1	$V_{oc}$ and $I_{sc}$ Variation with Thickness . . . . .	54
4.2	$V_{oc}$ and $I_{sc}$ Variations with Surface Recombination . . . . .	63
4.3	Lateral Voltage Drop as a Function of Depth . . . . .	64
4.4	Summary of I-V Curve Analysis . . . . .	69

## ABSTRACT

Presented here is a description of a lateral collection pin solar cell. An intrinsic region serves as the active generation region of the cell, thus allowing long diffusion lengths for the optically generated carriers. Collecting junctions are formed in isotropically etched grooves which traverse the thickness of the cell in a nearly vertical manner. A method for the fabrication of this silicon device is presented, and processing problems which were encountered are discussed. Testing of this solar cell was carried out in sunlight, and a method of determining the solar input power at the earth's surface based on the atmospheric attenuation is illustrated.

A mathematical model for this lateral collection device has been derived which accounts for the solar spectral distribution, atmospheric attenuation, and the silicon optical absorption coefficient. The ambipolar transport equation is solved by means of the Green's Function method to determine the distribution of the optically generated electron-hole pairs. Using this distribution, an analysis of the device arrives at a current-voltage characteristic from which the maximum output power, overall efficiency, and curve fill factor can be obtained. Computer solutions of the model are presented, and the results provide an insight to the effects of material parameters and device design on the overall performance of this pin solar energy converter.

## CHAPTER 1

### INTRODUCTION

Silicon junction solar energy conversion began in 1954 when Chapin, Fuller, and Pearson [1954] from Bell Telephone Laboratories fabricated the first p-n junction solar cell. While the efficiency of this cell was on the order of 6%, the prospects for this method of solar energy conversion were high. A maximum efficiency for a silicon junction device was predicted to be approximately 22% [Chapin, Fuller, and Pearson, 1954; Prince, 1955]. This predicted efficiency, along with the lightweight and high reliability of solid state devices, made the silicon solar cell a prime candidate as a power source for satellites and other space oriented projects.

With this impetus, research into the silicon solar cell flourished, but conversion efficiency fell somewhat short of the predicted maximum. While efficiencies as high as 15% have been achieved in research laboratories, production cells generally range from 10 to 12%. This apparent shortcoming can be attributed to several inherent limitations as discussed by Wolf [1960]. These limitations fall into two categories: those that are basic material limiting factors, and those that are technique or process limiting.

The factors limiting solar cell performance are:

1. Reflection losses on the surface
2. Incomplete photon absorption

3. Utilization of only part of the photon energy for electron hole pair production
4. Incomplete collection of the generated electron hole pairs
5. Squareness of the cell I-V curve defined by the Curve Fill Factor which is the ratio of maximum cell power output to the open circuit voltage times the short circuit current.
6. Output power losses due to internal series resistances.

Of the factors listed above, Nos. 2, 3, and 5 are basic material limiting factors arising from material properties or junction characteristics. The remaining three limitations can be minimized by appropriate geometries or fabrication techniques. As an example, addition of an antireflection coating will minimize the limitation of #1, whereas material of long lifetime or diffusion length will minimize the effect of #4. Wolf [1960] gives a complete discussion of the physical nature and implications of these limitations.

Present day commercial silicon solar cells typically consist of a square piece of 1  $\Omega$ -cm p-type silicon 2 cm on a side and approximately 10 mils thick. The p-n junction is formed by diffusing an n-type impurity into one of the faces to a depth of approximately 1 micron. Contacts are provided on both surfaces. On the dark or p-type side of the cell the entire surface is metallized providing a large area contact, while the illuminated face consists of a finger-like metal pattern to contact the n-type diffusion. Incident solar illumination produces a distribution of optically generated electron-hole pairs throughout the

silicon cell. Carriers within a diffusion length of the p-n junction are collected to contribute to the photo current. The remaining thickness of the solar cell does not contribute to the photo current, and thus, this portion of the cell is not active in solar energy conversion. Also, the metal contact on the top of the p-n junction cell does prevent some of the incident radiation from reaching the silicon material.

The structure and carrier collection of the pin solar energy converter differs from that of the conventional solar cell described above. The structure of the pin cell is illustrated in Fig. 1.1. The cell consists of a series of V-shaped grooves etched into the back side of the intrinsic silicon wafer. Alternate grooves are subsequently diffused p-type and the remaining grooves are diffused n-type, thereby forming the pin diode. Contacts are then provided on the n and p regions with like regions metallized together.

The purpose of the grooves is to distribute the p and n collecting junctions through most of the thickness of the cell, thus enabling collection of electron hole pairs which are generated near the illuminated surface as well as those generated deep in the material near the dark side of the cell. Use of intrinsic silicon in the generation region allows long carrier diffusion lengths because of the long carrier lifetime associated with the undoped material. The placement of the collecting junctions combined with the long diffusion length of the intrinsic material has the potential of an increased collection efficiency over the standard cell configuration. As the generated carriers are collected laterally, the collecting junctions must be placed within a carrier

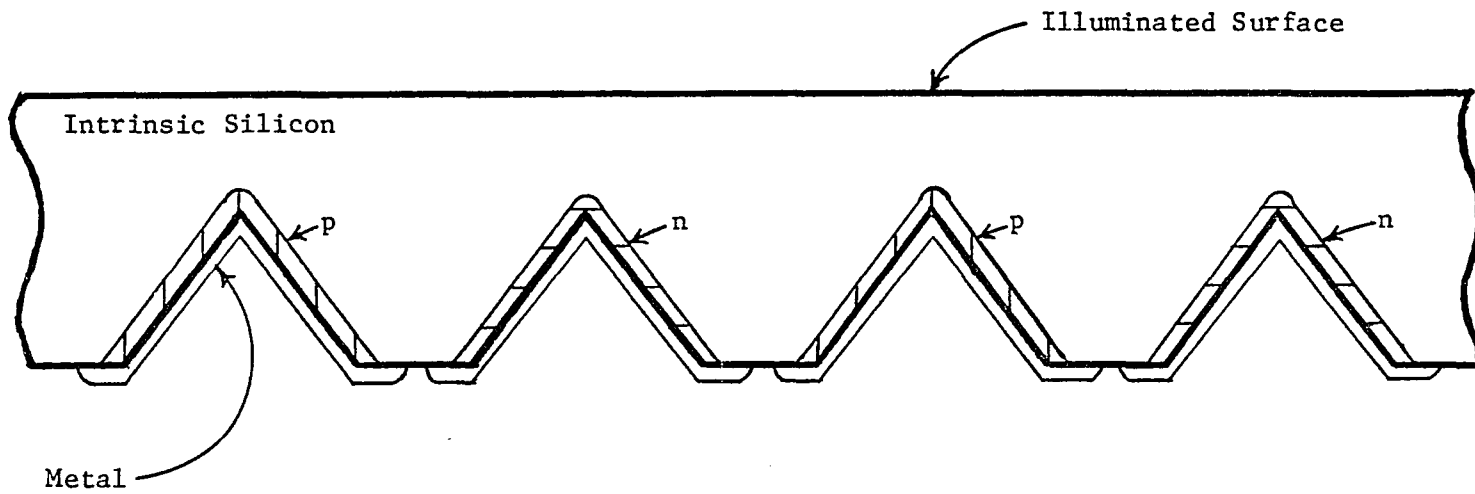


Fig. 1.1 PIN Solar Cell Profile

diffusion length apart to prevent electron hole pairs from being lost due to bulk recombination. All fabrication steps are performed on the dark side of the cell leaving the illuminated surface free of possible work damage. Also, the metallization for both contacts to the device are located on the dark side of the cell so there is no interconnecting pattern shadowing of the illuminated surface. Both p and n regions are heavily doped to provide low resistance regions and to assure ohmic contacts to the silicon.

Several solar cell analyses and configurations have been discussed in the literature. A thorough analysis of collection efficiencies for the conventional planar p-n junction solar cell was ~~carried out by~~ Kleinman [1961], where he considered the solar spectral photon distribution and the wavelength dependent absorption coefficient in the production of generated electron hole pairs. Ascribing appropriate boundary conditions based on carrier diffusion lengths, surface recombination velocities and carrier concentrations at the junctions, insight may be gained as to the effects of these parameters on collection efficiency. Evaluating collection efficiency as a function of the ratio of junction depth to diffusion length in the presence of extreme surface recombination velocities, Kleinman concluded that a junction depth of 1 micron is optimum for planar silicon solar cells. For such a cell constructed on silicon exhibiting a diffusion length of 100 microns, collection efficiencies range from .6 to .9 depending on the surface recombination velocities. Although this analysis is concerned with vertical collection devices and not the lateral collection as employed in the pin solar

cell, the effects of material parameters is illustrated, and a method of accounting for the spectral distribution and wavelength dependent absorption coefficient is presented.

A pin thermo-photovoltaic diode is described by Kim and Schwartz [1969] and is of a configuration closely resembling the pin structure described here. The Kim and Schwartz pin diode operates basically as a lateral collection device, but the collecting contacts are on the back or dark surface of the diode as shown in Fig. 1.2 rather than being projected into the cell. The analysis carried out by Kim and Schwartz for their cell structure is similar to that carried out for the pin solar energy converter described here with the exception that Kim and Schwartz used monochromatic incident radiation, thus avoiding the solar spectral distribution and the functional dependence of the absorption coefficient on wavelength. Also, their device was fabricated on germanium so that the numerical values of material parameters differ from those used in this study. Since the collecting contacts are placed on the planar back surface, the boundary conditions placed on the partial differential equation solution also are different.

The pin structure with lateral collection was investigated by Johnson [1970], where a constant generation rate was assumed throughout the intrinsic region. This assumption considerably simplified the analysis since a one-dimensional solution would suffice, and the solar spectral distribution as well as the wavelength dependent absorption coefficient did not need to be directly taken into account. Expressions were derived for the junction potentials for the open circuit condition

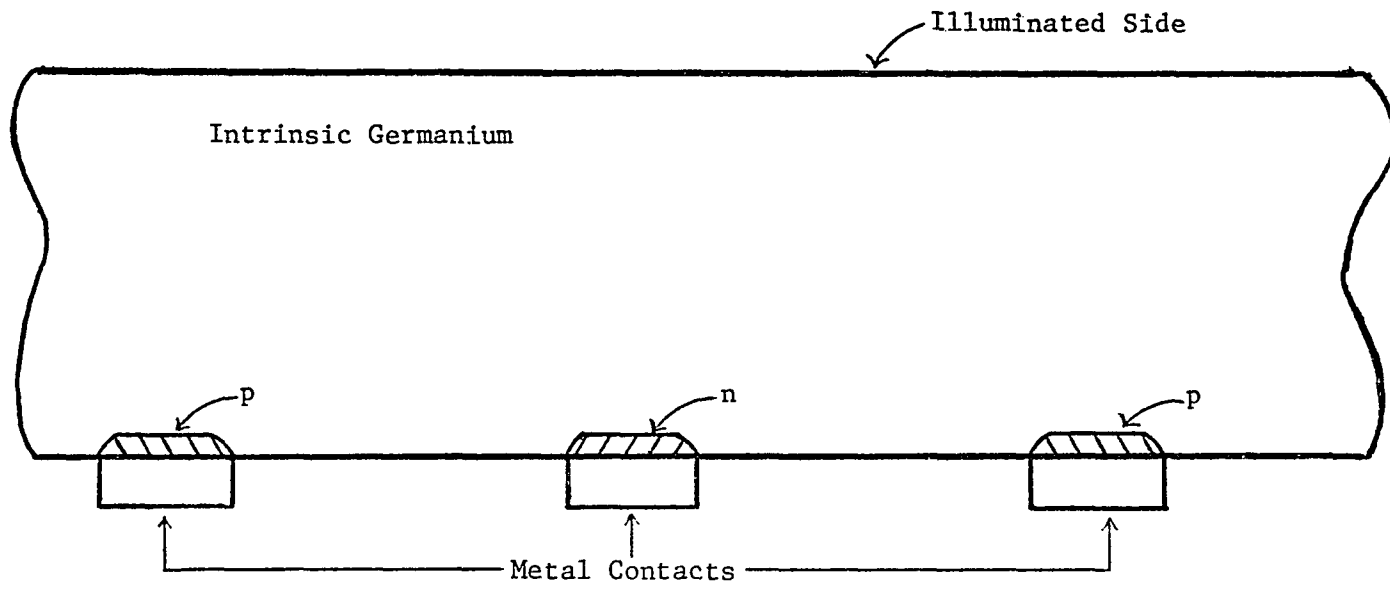


Fig. 1.2 PIN Diode of Kim and Schwartz [1969]

and the maximum output power density. Upon substitution of assumed device and material parameters, calculated values for the open circuit voltage and output power were obtained. The generation rate assumed in these calculations was several orders of magnitude too high yielding an unusually high conversion efficiency. Assumption of a more appropriate generation rate results in an unusually low efficiency.

Analyses carried out by Kleinman [1961], and Kim and Schwartz [1969], point out several important parameters that need be applied to the structure investigated by Johnson [1970]. The two-dimensional analysis described here takes into account the solar spectral distribution, wavelength dependent absorption coefficient, and arbitrary surface recombination velocities at both the illuminated and dark side of the cell. This analysis is presented in Chapter 3. Numerical analyses were made with the CDC 6400 digital computer located at The University of Arizona Computer Center, and results from these calculations are discussed in Chapter 4. The details of the solar cell fabrication are given in the following chapter.

## CHAPTER 2

### DEVICE FABRICATION AND TEST

#### Fabrication

The pin solar cells were fabricated in The University of Arizona Solid State Engineering Laboratory which provided many of the required processes as well as a maskmaking facility. Among the processes provided were the standard diffusion processes and the metallization process.

The diffusions were of the two step type, i.e., deposition and drive-in. Both boron and phosphorus were deposited at 1050°C using gaseous sources. Drive-in was performed at 900°C in a steam ambient. The boron deposition is characterized by the complementary error function distribution with a boron surface concentration of  $3 \times 10^{20} \text{ cm}^{-3}$  and a diffusion length of  $3.7 \times 10^{-3} \text{ } \mu\text{m}$ . The phosphorous deposition is characterized by a phosphorous surface concentration of  $2 \times 10^{21} \text{ cm}^{-3}$  and a diffusion length of  $3.1 \times 10^{-3} \text{ } \mu\text{m}$ . The n-type impurity profile is again described by the complementary error function distribution. Drive-in times were picked to give sufficient oxide growth to facilitate the subsequent process steps. A two hour boron drive-in results in a 3000 Å oxide to mask against the subsequent phosphorous diffusion, whereas a 75 minute phosphorous drive-in yields a 2000 Å oxide which is necessary to convert the phosphorsilicate glass to a form which has better photoresist adherence properties. Despite the relatively long

drive-in times, the diffusion coefficients of boron and phosphorus at the 900°C drive-in temperature are sufficiently low so that negligible diffusion results.

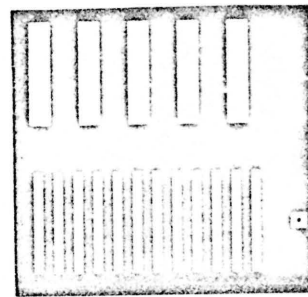
Another established process which was used for the solar cell fabrication was that of the aluminum metallization. This process is the standard filament evaporation of high purity aluminum followed by a sinter to increase the adhesion between the silicon wafer and the metal as well as to form the contacts on the doped regions of the cell. The sinter is carried out at 500°C for 10 minutes in a forming gas atmosphere.

The integrated circuits laboratory also provided the capability for the mask layout and the mask production. Artwork for the masks were generated on Rubylith using a precision cutting table. The artwork was then photoreduced by a factor of ten and this first reduction image was stepped and repeated in a contact printing process to produce a 5x5 array of images on a photographic film. After developing and drying, this film was further reduced to achieve a total reduction of 125. It is this second reduction that produces the working set of masks which are used in the photoresist process.

The masks which were drawn up to fabricate the solar cells consisted of two different groove spacings but with approximately equal areas. The purpose of this was to provide cells of sufficiently different size to assess the influence of groove width and spacings on cell efficiency. The mask set for the two cell geometries are shown in Fig. 2.1.



Groove Windows and  
Contact Windows



Boron Diffusion



Phosphorous Diffusion



Metallization

Fig. 2.1 Mask Set

The large groove cells have an area of  $3.22 \times 10^{-6} \text{ m}^2$  or 48 mils x 104 mils, and the grooves are spaced on 10 mil centers. The width of the window openings are 6 mils x 40 mils which results in a groove depth of 4.5 mils. In contrast, the small groove cells occupy an area of  $3.03 \times 10^{-6} \text{ m}^2$  or 48 mils x 98 mils, and the grooves are spaced on 4 mil centers. The window openings which are 2 mils x 40 mils produce an etched groove 1.5 mils deep. This small geometry cell represents the minimum size which can be achieved with the existing laboratory capabilities.

In addition to the available IC processes described above, two additional processes needed to be developed. These are:

1. the characterization of the anisotropic or preferential silicon etch, and
2. the development of the subsequent photoresist procedures for the non-monolithic surface.

The preferential etch was employed to form the grooves in the silicon wafers and consisted of a water-amine-complexing agent of the type described by Finne and Klein [1967]. This etch was carried out in a glass refluxing system with nitrogen bubbling through the etchant to provide agitation and an inert atmosphere. The preferential nature of this etch is that the etch rate into the  $\langle 100 \rangle$  planes of the silicon is significantly larger than the etch rate into the  $\langle 111 \rangle$  planes. In effect, the  $\langle 111 \rangle$  planes act as terminators for the etch. An etch rate in the  $\langle 100 \rangle$  silicon of 40  $\mu\text{m}$  per hour was achieved at 95°C yielding a groove defined by the  $\langle 111 \rangle$  planes which meet the surface

at an angle of approximately  $54^\circ$ . Measurements of this angle were in good agreement with crystallographic predictions. Silicon dioxide is not significantly affected by this water-amine etch.

The  $\langle 111 \rangle$  planes which form the groove walls intersect the surface of the wafer at right angles. To maintain the groove dimensions, it is necessary that the mask which defines the grooves be properly aligned along these crystal planes. A slight misalignment enlarges the grooves and produces bowed edges as shown in Fig. 2.2. Since the wafers used for the fabrication of these cells did not have crystal orientation reference flats, a method was developed to determine the crystal orientation. The method was to cut a series of round holes through the thermal oxide on the periphery of the wafer and then subject the wafer to the preferential silicon etch. The effect of the etch was to form a pit in the silicon in the shape of an inverted pyramid; the four sides of this etched pit are the  $\langle 111 \rangle$  planes to which alignment can be made. The standard monolithic photoresist process was then repeated to define the windows in the thermal oxide for the grooves, and the grooves were then etched.

The grooves which result from the anisotropic etch exhibit a rather sharp edge at the wafer surface. To aid the subsequent photoresist adhesion, it is necessary to round or smooth these sharp corners. Following the etching of the grooves, the oxide on the grooved side of the wafer was removed and the wafer was etched in an isotropic etch consisting of HF,  $\text{HNO}_3$  and acetic acid for 30 seconds. The effect of this step is shown in Fig. 2.3. The wafer was then reoxidized.

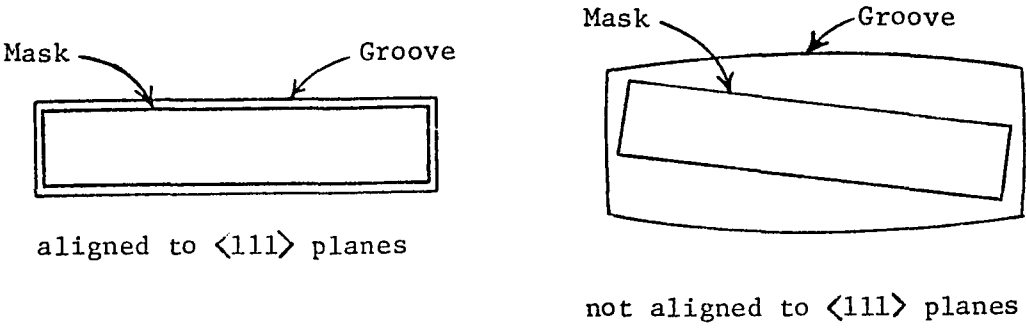


Fig. 2.2 Effect of Mask Alignment to  $\langle 111 \rangle$  Planes on Groove Dimensions

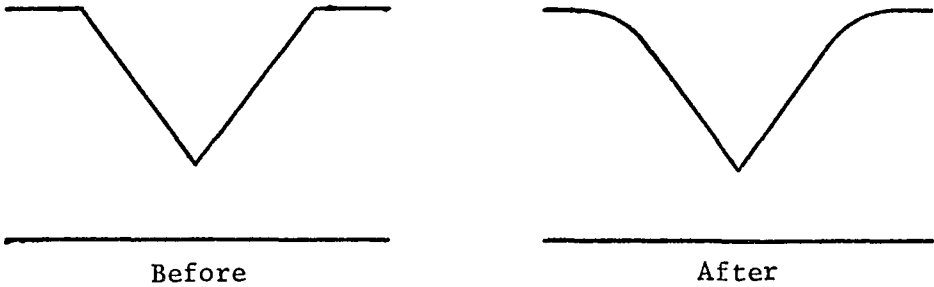


Fig. 2.3 Groove Profile Before and After  $\text{HF}:\text{HNO}_3:\text{HAc}$  Etch

After the grooves were etched and the wafer reoxidized, it was necessary to remove the oxide in alternate grooves and perform the p diffusion, then remove the oxide in the remaining grooves and perform the n diffusion to form the pin structure. The standard monolithic photoresist process of spinning the resist to a thin even coat cannot be used on the non-monolithic surface of this solar cell because the spinning results in a separation of the photoresist at the corners of the groove as depicted in Fig. 2.4. Drip applications of photoresist of various viscosities were tried as another approach. However, when sufficient resist was applied to keep the corners covered, the resulting resist thickness on the surface could not be properly exposed to give reasonable line definition or complete development. Particularly, if a long expose time was used, the resist in the groove would not fully develop out, while for short expose times the resist would not fully polymerize and would flow into the unexposed areas during developing, thus destroying edge definition. From this, it became obvious that the resist on the surface must be thin to produce acceptable line definition, but at the same time, the resist in the grooves must be thick to assure edge coverage.

An alternative approach which was then explored was to fill the grooves and then apply a relatively thin coat of resist by spinning. To accomplish this, photoresist was drip applied to the wafer and the excess removed with a Teflon squeegee. This wipes the surface clean leaving resist in the grooves. When the grooves are filled, a thin coat of

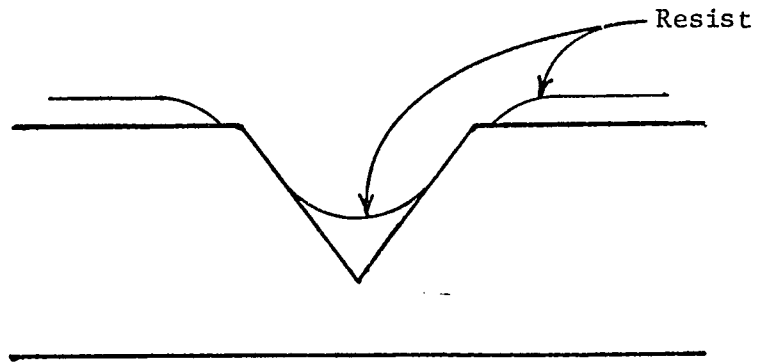


Fig. 2.4 Separation of Resist at the Corners of the Groove

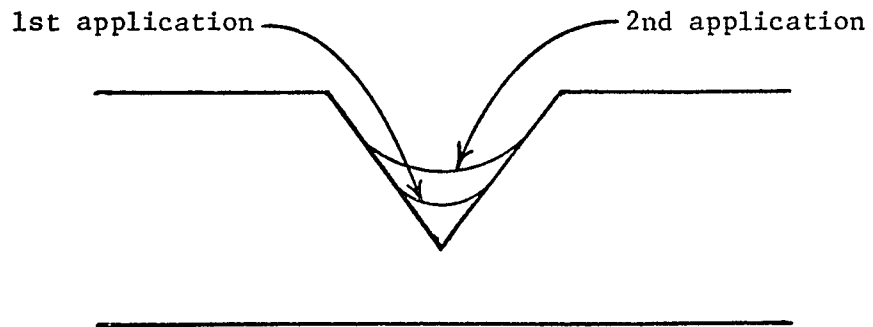


Fig. 2.5 Resist Build-up Due to Multiple Application

resist can be applied by the conventional spinning procedure. The successful process is as follows:

1. Apply resist and squeegee. Dry at 90°C for 10 minutes.
2. Apply resist and squeegee. Dry at 90°C.
3. Align mask and expose for 10 seconds.
4. Apply resist and squeegee. Dry at 90°C for 10 minutes.
5. Align mask and expose for 10 seconds.
6. Apply resist and spin 0-5000 rpm. Dry at 90°C for 10 minutes.
7. Align mask and expose for 30 seconds.
8. Dip develop for 2 minutes.
9. Post bake at 125°C for 25 minutes.

The repeated exposures in the above described procedure are necessary to polymerize the resist near the corners of the grooves and so allow the resist to build up to insure that the spin coating will cover these corners. This resist buildup within the groove is pictured in Fig. 2.5.

The above process yields acceptable edge definition, but presents a developing problem if misalignment occurs in any of the expose steps. Such a misalignment on one edge of the groove causes polymerization of the resist on the opposite wall of the groove as shown in Fig. 2.6. When this occurs, the cell is carried through the remaining steps in the photoresist process and through the oxide etch. The wafer is then cleaned and dried, and the photoresist procedure as outlined above is repeated a second time so that the entire groove is free of the strip of unwanted masking oxide.

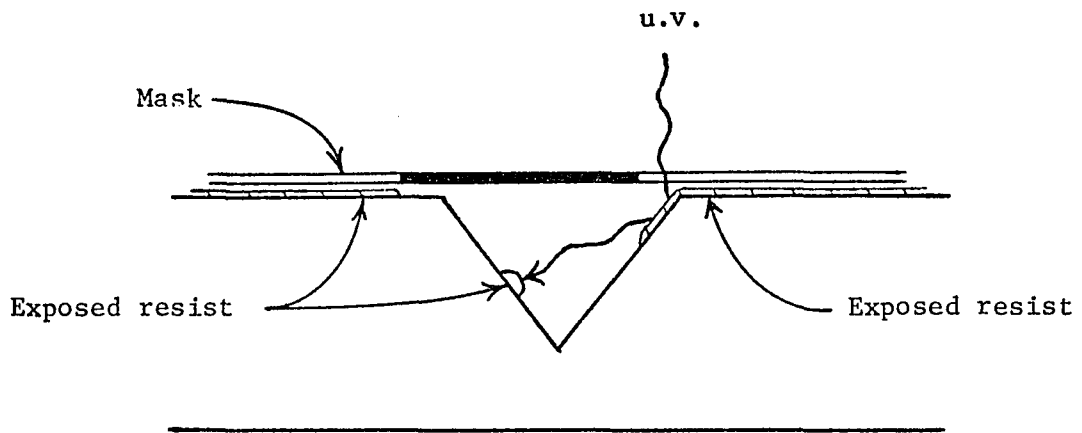


Fig. 2.6 Result of Mask Misalignment on Polymerization of Resist

The photoresist procedure is somewhat simpler for the metallization pattern, and it consists of the following steps:

1. Sinter the aluminum for 10 minutes at 500°C.
2. Spin on photoresist at 7000 rpm and dry at 90°C for 10 minutes.
3. Align metallization mask and expose for 10 seconds.
4. Spin on photoresist at 5000 rpm and dry at 90°C for 10 minutes.
5. Align metallization mask and expose for 10 seconds.
6. Dip develop and post bake at 125°C for 25 minutes.

The sintered aluminum has a rough texture which is characteristic of large grain size. Thus the aluminum texture is considerably rougher than the surface of the  $\text{SiO}_2$  causing the photoresist to adhere much better.

At this point in the fabrication of the solar cell, the pin structure is completed. The above fabrication processes were performed on silicon wafers 10 mils thick with V-grooves etched into the dark side of the cells to a depth of either 4.5 mils or 1.5 mils. For the cells to operate effectively, the wafers must be thinned so that the illuminated surface of the cell is in close proximity to the peaks of the grooves. The thinning was performed by waxing the wafers to glass microscope slides and subjecting the wafers to an isotropic silicon etchant. The etchant was mixed in the following proportions:

HF	-	10 ml.
$\text{HNO}_3$	-	5 ml.
Acetic Acid	-	14 ml.

The wafers were agitated in this mixture resulting in an etch rate of about 1 mil per minute. This process was performed for different time

intervals to provide wafers or cells of varying thickness so as to assess the influence of wafer thickness on cell efficiency.

### Test

The completed solar cells were mounted on a probe station within a box which was constructed to permit testing of the cells by directly illuminating them with sunlight while making electrical contact via probes to the back side of the wafer. The illumination inlet on the box was apertured and baffled so that the cells under test could only receive directly transmitted solar radiation, and the box was manually steered to track the sun during testing. A sketch of the test station is shown in Fig. 2.7.

Direct solar radiation was used for making the cell evaluation because it was felt that a more accurate assessment of cell efficiency could be made using sunlight rather than using simulated sources, weighting spectral scans, computer integration, etc. The basis for this may be better understood if one examines the solar transmission equation which may be put in the form

$$F(\lambda) = F_o(\lambda) e^{-\tau(\lambda)\sec\phi} \quad , \quad (2.1)$$

where  $F(\lambda)$  is the directly transmitted solar energy at wavelength  $\lambda$  received at the earth's surface,  $F_o(\lambda)$  is the corresponding value at the top of the atmosphere (at airmass zero, or  $\tau(\lambda) = 0$ ),  $\tau(\lambda)$  is the total optical depth at wavelength  $\lambda$  referenced to the zenith, and  $\sec\phi$  is an airmass factor which determines the increased optical path which a solar ray traverses at zenith angle  $\phi$  relative to that traversed by a ray

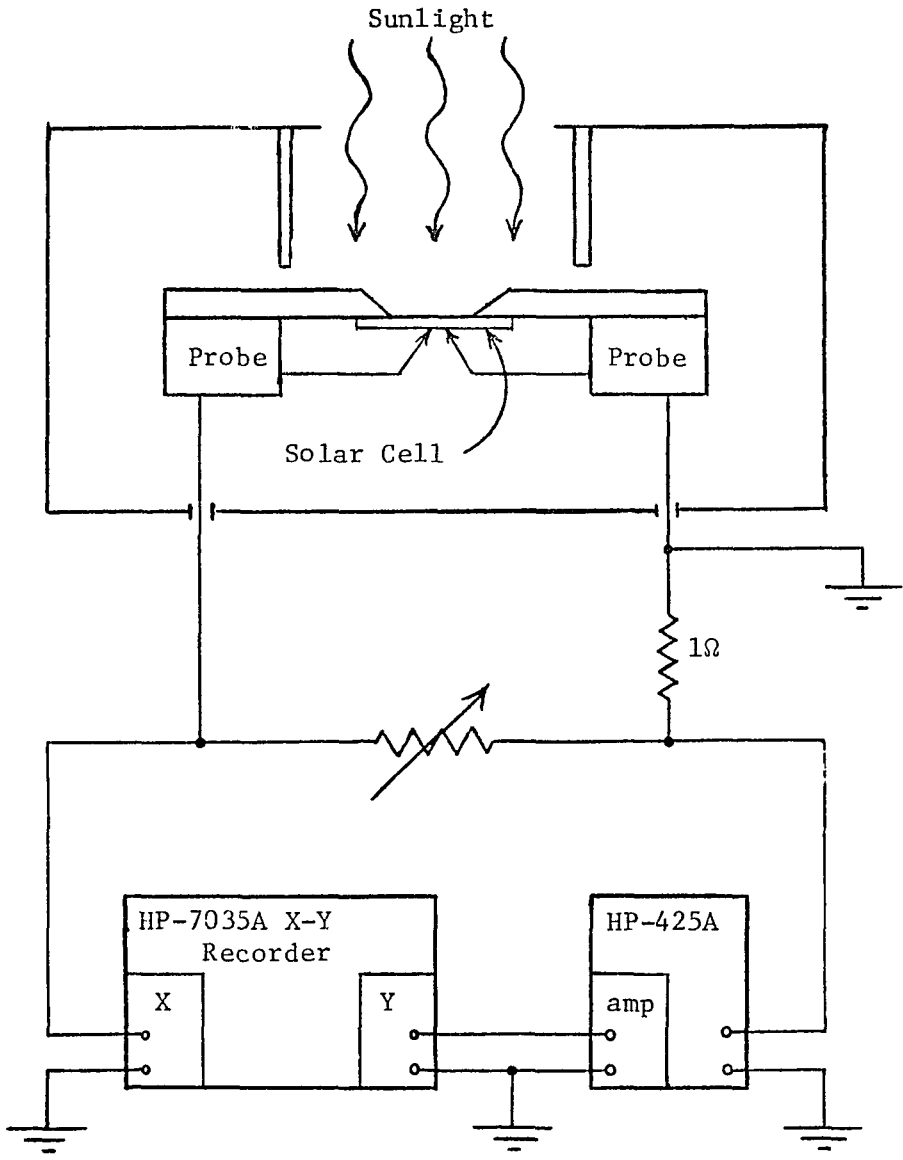


Fig. 2.7 PIN Solar Cell Test Set

entering the atmosphere at the zenith. This expression is quite valid for zenith angles well above the horizon and for relatively clear atmospheres such as those typically observed in Tucson [Shaw, 1971; Shaw, Reagan, and Herman, 1973]. The factor  $F_0(\lambda)$  is now known accurately on the basis of spectral measurements of the solar constant by several investigators. Recent results reported by Thekaekara [1970] are considered the most accurate, and his results yield a total solar input at the top of the atmosphere of  $135.1 \text{ mw cm}^{-2}$  for the mean earth-sun distance.

Knowing  $F_0(\lambda)$ , the solar spectral response at the earth surface,  $F(\lambda)$ , may accurately be determined if the total optical depth,  $\tau(\lambda)$ , is known. The optical depth accounts for attenuation due to molecular scattering, molecular absorption, and particulate scattering and absorption. The contributions due to molecular scattering and absorption are well known and may be obtained from model atmosphere tables, whereas the particulate contribution is generally unknown. However, a unique multi-wavelength solar radiometer is now operating on a daily basis in Tucson. Results from the radiometer measurements have been compiled by Shaw [Shaw, 1971; Shaw et al., 1973] to determine the average particulate optical depth contribution for good clear days in Tucson. Making use of this information along with standard atmosphere information, the ground-level solar spectral distribution in Tucson can be fairly accurately determined. Numerically integrating the resulting distribution, it has been determined that the total solar input at the

surface in Tucson for good clear dry days is  $105 \pm 5 \text{ mw cm}^{-2}$  at the mean earth-sun distance for the zenith angle  $\phi = 0^\circ$ .

Using the above surface level solar input value, corrections were made for the actual zenith angle and earth-sun distance on the day and time that a given cell was tested. It should be noted that such correction information is readily available from tables and charts, and it does not add any significant complexity to the calibration procedure. Tests were performed on only good clear days, and the tests were also made near local noon so that the solar zenith angle would be close to the minimum obtainable angle for the day in question. Considering all errors associated with determining the solar input on the test cells, it was estimated that cell efficiency could be accurately inferred to about  $\pm 0.5\%$  for efficiency levels typical of those determined for the test cells (i.e., efficiencies of approximately 10%).

Cell measurements were made for various wafer thicknesses by first testing the cells at their original wafer thickness (10 mils) and then repeatedly subjecting the cells to the etch thinning process while retesting the cells after each thinning. In this fashion, it was possible to reduce the thickness of the cell wafers to as little as 2.5 mils (for small groove cells only). Further thinning would cause the cells to break apart due to the grooves reaching the front surface. In addition, most of the cells were tested for two surface treatment cases, namely,

1. illuminated surface left bare after etch treatment, and

2. illuminated surface coated with a boron doped spin-on diffusion source.

It should be noted that the boron coating was not used as a diffusion source in this case. It was found, somewhat by accident, that this coating generally improved cell performance. Details concerning test results will be presented in Chapter 4.

## CHAPTER 3

### THEORETICAL ANALYSIS

The aim of the theoretical analysis is to arrive at a meaningful model to assess the performance of the previously described pin solar cell. Specifically, the voltage-current characteristic under solar illumination will be determined, and from this, the maximum output power and curve fill factor will be obtained. To this end, the ambipolar transport equation will be solved by means of the Green's Function Method to arrive at the density of optically generated electron-hole pairs. From this carrier distribution, the current voltage characteristic can be established.

The principle of operation of the pin solar cell is that solar illumination generates electron-hole pairs within the intrinsic region. The internal fields at the p-i and n-i junctions are such that holes which diffuse into the p-i depletion region are swept toward the p region. Electrons are collected in a similar fashion at the n region. This flow of electrons and holes gives rise to the photo generated current and/or voltage. This voltage or current can be calculated with a knowledge of the distribution of photo generated electron hole pairs. To determine this distribution, the ambipolar transport equation, with the appropriate generation term, must be solved. The steady state ambipolar transport equation applied to the intrinsic region of the cell may be written as

$$D^* \nabla_{xy}^2 n(x,y) + G - R = 0 \quad (3.1)$$

where  $D^*$  is the ambipolar diffusion coefficient,  $G$  the solar generation rate,  $R$  the bulk recombination and  $n(x,y)$  is the distribution of optically generated carriers.

The generation of electron-hole pairs by photon absorption is described by Lambert's absorption law which, when expressed over the useful portion of the spectrum, gives

$$G(x) = \int_{\lambda_1}^{\lambda_2} \alpha(\lambda) N(\lambda) e^{-\alpha(\lambda) x} d\lambda \quad (3.2)$$

The short wavelength limit of the solar spectrum is defined by  $\lambda_1$ , and  $\lambda_2$  represents the cutoff wavelength of the silicon corresponding to the bandgap energy. The absorption coefficient,  $\alpha(\lambda)$ , is a function of wavelength as is the density of photons,  $N(\lambda)$ , in the solar spectrum output. The distance into the silicon from the illuminated surface is denoted by the variable  $x$ . The generation rate,  $G(x)$ , is expressed in carriers per  $\text{cm}^3$  per second. The recombination term  $R$  is expressed in the same units and is written as

$$R(x,y) = \frac{n(x,y)}{\tau} \quad , \quad (3.3)$$

where  $\tau$  is the bulk carrier lifetime in the intrinsic region. Using the above terms, the ambipolar transport equation becomes

$$D^* \nabla_{xy}^2 n(x,y) - \frac{n(x,y)}{\tau} = - \int_{\lambda_1}^{\lambda_2} \alpha(\lambda) N(\lambda) e^{-\alpha(\lambda)x} d\lambda \quad (3.4)$$

For simplification, a rectangular geometry will be used for the device analysis. Figure 3.1 illustrates the assumed geometry and coordinate system which will be used in the following analysis. The boundary conditions governing the intrinsic region are arbitrary surface recombination at the illuminated surface,  $x = 0$ , and on the dark surface  $x = a$ . These are expressed as

$$\left. \frac{\partial n}{\partial x} \right|_{x=0} = \frac{S_0}{D^*} n(0,y) \quad (3.5)$$

for the illuminated surface, and

$$\left. \frac{\partial n}{\partial x} \right|_{x=a} = - \frac{S_a}{D^*} n(a,y) \quad (3.6)$$

on the dark surface of the cell. The terms  $S_0$  and  $S_a$  denote the surface recombination velocities at  $x = 0$  and  $x = a$ , respectively. The boundary conditions for the  $y$  coordinates specify the carrier density at the intrinsic side of the junctions. These concentrations are assumed to be independent of the  $x$  coordinate, but are dependent on the junction potentials. The density expression at the intrinsic side of the p-i junction is given by

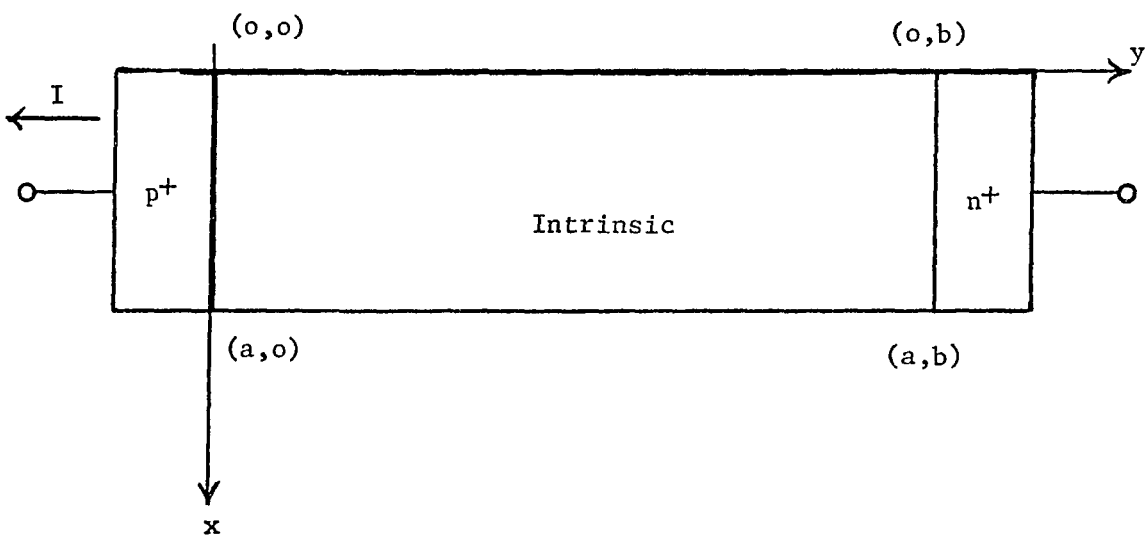


Fig. 3.1 Geometry and Coordinate System Used in Analysis

$$n(x,0) = n_i \left( e^{qV_p/kT} - 1 \right) = U(V_p), \quad (3.7)$$

where  $V_p$  is the p-i junction potential. The corresponding density at the n-i junction is given by

$$n(x,b) = n_i \left( e^{qV_n/kT} - 1 \right) = V(V_n). \quad (3.8)$$

The above boundary conditions on  $y$  appear to be somewhat vague at this point; however, actual values for  $U$  and  $V$  will be determined later when the pin device is analyzed.

The solution of the ambipolar transport Eq. (3.4) subject to the boundary conditions (Equations 3.5 - 3.8) yields the distribution of the optically generated electron-hole pairs. To obtain this distribution, the Green Function approach will be followed. For the moment, let's generalize the problem and rewrite the partial differential equation (PDE) and boundary conditions in a simpler, more general form. The PDE becomes

$$\text{Ln} = f(x,y) \quad (3.9)$$

The general form of the boundary conditions are:

$$n'(0,y) = \alpha n(0,y) \quad (3.10)$$

$$n'(a,y) = -\beta n(a,y) \quad (3.11)$$

$$n(x,0) = U \quad (3.12)$$

$$n(x,b) = V \quad (3.13)$$

The Green's Function,  $g$ , is expressed

$$Lg(x,y) = \delta(x-x')\delta(y-y') \quad (3.14)$$

where the operator  $L$  in Eq. (3.9) and (3.14) is

$$L = \nabla_{xy}^2 + \frac{1}{\tau} \quad (3.15)$$

To obtain the Green's Function for the two-dimensional region, first consider the inner products

$$\langle n, Lg \rangle = \langle n, \delta(x-x')\delta(y-y') \rangle = n(x',y') \quad (3.16)$$

and

$$\langle Ln, g \rangle = \langle f, g \rangle \quad (3.17)$$

Taking the difference,

$$\langle n, Lg \rangle - \langle Ln, g \rangle = n(x',y') - \langle f, g \rangle \quad (3.18)$$

where  $n(x',y')$  is the solution to Eq. (3.9) and  $\langle f, g \rangle$  is the integral of the forcing function with the Green's Function. Expansion of the terms on the left hand side with the application of the boundary condition 3.10 - 3.13 results in boundary terms for the solution to 3.9.

Specifically, the PDE for the Green's Function  $g$  is

$$\nabla_{xy}^2 g(x,y|x',y') - \frac{1}{L^{*2}} g(x,y|x',y') = \delta(x-x')\delta(y-y') \quad (3.19)$$

where  $L^* = \sqrt{D^*\tau}$  is the ambipolar diffusion length, and the associated boundary conditions for the Green's Function are

$$\left. \frac{\partial g}{\partial x} \right|_{x=0} = \frac{S_o}{D^*} g \Big|_{x=0} \quad (3.20)$$

$$\left. \frac{\partial g}{\partial x} \right|_{x=a} = -\frac{S_a}{D^*} g \Big|_{x=a} \quad (3.21)$$

$$g \Big|_{y=0} = 0 = g \Big|_{y=b} \quad (3.22)$$

The total solution to Eq. (3.9) becomes

$$n(x,y) = \langle f, g \rangle - U \int_0^a \left. \frac{\partial g}{\partial y} \right|_{y'=0} dx' - V \int_a^0 \left. \frac{\partial g}{\partial y} \right|_{y'=b} dx' \quad (3.23)$$

To obtain the Green's Function, an expansion in the y dimension is formed.

$$g(x,y|x',y') = \sum_n a_n(x) \sqrt{\frac{2}{b}} \sin \frac{n\pi y}{b} \quad (3.24)$$

and

$$\delta(y-y') = \sum_n \sqrt{\frac{2}{b}} \sin \frac{n\pi y}{b} \sqrt{\frac{2}{b}} \sin \frac{n\pi y'}{b} \quad (3.25)$$

These two equations are substituted into Eq. (3.19), and, using the orthogonality of the sin functions, an expression for the coefficients  $a_n$  is obtained. This expression is of the form of 3.14, but in one dimension. Following the Green's Function method, the coefficient is found. The resulting Green's Function is

$$g_1(x,y|x',y') = \sum_m -\eta \left[ \frac{K_a \sinh \frac{x'}{\eta} + \cosh \frac{x'}{\eta}}{\frac{K_a D^*}{\eta S_0} - 1} \right] \left[ \sinh \frac{x}{\eta} + \frac{D^*}{\eta S_0} \cosh \frac{x}{\eta} \right] \cdot$$

$$\frac{2}{b} \sin \frac{m\pi y'}{b} \sin \frac{m\pi y}{b} \quad \text{for } x < x' \quad (3.26)$$

and

$$g_2(x,y|x',y') = \sum_m -\eta \left[ \frac{\sinh \frac{x'}{\eta} + \frac{D^*}{\eta S_0} \cosh \frac{x'}{\eta}}{\frac{K_a D^*}{\eta S_0} - 1} \right] \left[ K_a \sinh \frac{x}{\eta} + \cosh \frac{x}{\eta} \right] \cdot$$

$$\frac{2}{b} \sin \frac{m\pi y'}{b} \sin \frac{m\pi y}{b} \quad \text{for } x > x' \quad (3.27)$$

In the above expressions,  $\eta$  and  $K_a$  are defined as

$$\frac{1}{\eta^2} = \left(\frac{n\pi}{b}\right)^2 + \frac{1}{L^{*2}} \quad (3.28)$$

and

$$K_a = -\frac{\frac{1}{\eta} \sinh \frac{a}{\eta} + \frac{S_a}{D^*} \cosh \frac{a}{\eta}}{\frac{1}{\eta} \cosh \frac{a}{\eta} + \frac{S_a}{D^*} \sinh \frac{a}{\eta}} \quad (3.29)$$

With the Green's Function at hand, the density of optically generated carriers can be found from Eq. (3.23). For simplicity, Eq. (3.23) can be written as

$$n(x,y) = A(x,y) + U B(x,y) + V C(x,y) \quad (3.30)$$

where

$$A(x,y) = \langle f, g \rangle = \iint_{xy} \left[ \frac{\tau}{L^2} \int_{\lambda_1}^{\lambda_2} \alpha(\lambda) N(\lambda) e^{-\alpha(\lambda)x'} d\lambda \right] g(x,y|x',y') dx' dy' \quad (3.31)$$

$$B(x,y) = - \int_0^a \frac{\partial g}{\partial y} \Big|_{y'=0} dx' \quad (3.32)$$

and

$$C(x,y) = - \int_a^0 \left. \frac{\partial g}{\partial y} \right|_{y'=b} dx' \quad (3.33)$$

The function  $A(x,y)$  is the density term arising from carrier generation stimulated by an optical source which has a photon spectrum described by  $N(\lambda)$ . The remaining functions  $B(x,y)$  and  $C(x,y)$  are density terms which arise from the presence of junctions at the edges of the intrinsic region of the solar cell.

The first term of the density expression can be integrated to obtain the actual functional form of the optically generated carriers. By interchanging the order of integration and evaluating the spatial integrals, the expression for  $A$  becomes

$$A(x,y) = \frac{\tau}{L^*} \sum_m \frac{4\eta^2}{m\pi} \sin \frac{m\pi y}{b} \left\{ \int_{\lambda_1}^{\lambda_2} \frac{N\alpha}{1-\alpha^2\eta^2} e^{-\alpha x} d\lambda + \frac{K_a \sinh \frac{x}{\eta} + \cosh \frac{x}{\eta}}{K_a D^* - \eta S_o} \right.$$

$$\int_{\lambda_1}^{\lambda_2} \frac{N\alpha\eta}{1-\alpha^2\eta^2} (S_o + D^*\alpha) d\lambda - \frac{\eta S_o \sinh \frac{x}{\eta} + D^* \cosh \frac{x}{\eta}}{K_a D^* - \eta S_o} \left[ \cosh \frac{a}{\eta} + K_a \sinh \frac{a}{\eta} \right] \cdot$$

$$\left. \int_{\lambda_1}^{\lambda_2} \frac{N\alpha^2\eta}{1-\alpha^2\eta^2} e^{-\alpha a} d\lambda + (\sinh \frac{a}{\eta} + K_a \cosh \frac{a}{\eta}) \int_{\lambda_1}^{\lambda_2} \frac{N\alpha}{1-\alpha^2\eta^2} e^{-\alpha a} d\lambda \right\} \quad (3.34)$$

Integration over the spectral density can be carried out analytically if  $N(\lambda)$  is a known function. Although  $N(\lambda)$  has been empirically determined for the solar spectrum [Thekaekara, 1970], it is not easily fitted to an analytic function. Instead, numerical integration can be incorporated.

The boundary terms,  $B(x,y)$  and  $C(x,y)$  can be found by carrying out the operations described by Equations (3.32) and (3.33) to get

$$B(x,y) = \sum_{m=1}^{\infty} \frac{2m\pi\eta^2}{b} \sin \frac{m\pi y}{b} \left\{ \frac{1}{K_a D^* - \eta S_o} \left[ K_a \eta S_o \sinh \frac{x}{\eta} (\cosh \frac{a}{\eta} - 1) \right. \right. \\ \left. \left. + D^* \cosh \frac{x}{\eta} (\sinh \frac{a}{\eta} + K_a \cosh \frac{a}{\eta}) + \eta S_o (\sinh \frac{x}{\eta} \sinh \frac{a}{\eta} - \cosh \frac{x}{\eta}) \right] - 1 \right\} \quad (3.35)$$

and

$$C(x,y) = - \sum_{m=1}^{\infty} (-1)^m \frac{2m\pi\eta^2}{b} \sin \frac{m\pi y}{b} \left\{ \frac{1}{K_a D^* - \eta S_o} \left[ K_a \eta S_o \sinh \frac{x}{\eta} (\cosh \frac{a}{\eta} - 1) \right. \right. \\ \left. \left. + D^* \cosh \frac{x}{\eta} (\sinh \frac{a}{\eta} + K_a \cosh \frac{a}{\eta}) + \eta S_o (\sinh \frac{x}{\eta} \sinh \frac{a}{\eta} - \cosh \frac{x}{\eta}) \right] - 1 \right\} \quad (3.36)$$

The functional form of the optically generated electron hole pairs is thus known to within the constants  $U$  and  $V$  in Eq. (3.30). These constants can be found by examining the device operation.

At this point, we have evaluated the carrier density in the intrinsic region of the pin solar cell. Actual carrier concentrations can be obtained by numerical computation carried out by a computer. Let us now proceed to analyze the solar cell to determine the voltage-current characteristic. From this, the open circuit voltage, short circuit current, maximum power output, efficiency, and curve fill factor can be found.

To begin the characterization of this device, the current flow resulting from the optically generated carriers will be determined in terms of the excess carrier density in the intrinsic region. Consider the p-i junction of Fig. 3.1. The field in the depletion region is directed so that any holes which diffuse from the intrinsic region into the depletion region are swept across this region to the heavily doped p contact. Because of this field direction, the electrons will not traverse the depletion region, which indicates that

$$J_n(x,0) = 0, \quad (3.37)$$

but

$$J_n(x,0) = q\mu_n E(x,0)n(x,0) + qD_n \left. \frac{\partial n(x,y)}{\partial y} \right|_{y=0} \quad (3.38)$$

so

$$E(x,0) = - \frac{kT}{q} \frac{1}{n(x,0)} \left. \frac{\partial n(x,y)}{\partial y} \right|_{y=0}, \quad (3.39)$$

where the Einstein's relation  $\frac{D}{\mu} = \frac{kT}{q}$  has been employed. Writing the current density equation for holes

$$J_p(x,0) = q\mu_p n(x,0) E(x,0) - qD_p \left. \frac{\partial n(x,y)}{\partial y} \right|_{y=0} \quad (3.40)$$

and substituting for  $E(x,0)$  from Eq. (3.39),

$$J_p(x,0) = -q \frac{kT \mu_p}{qn(x,0)} n(x,0) \left. \frac{\partial n(x,y)}{\partial y} \right|_{y=0} - qD_p \left. \frac{\partial n(x,y)}{\partial y} \right|_{y=0} \quad (3.41)$$

or

$$J_p(x,0) = -2qD_p \left. \frac{\partial n(x,y)}{\partial y} \right|_{y=0}. \quad (3.42)$$

Substituting Eq. (3.30) for  $n(x,y)$  into Eq. (3.42), we obtain

$$J_p(x,0) = -2qD_p [A_y(x,0) + U B_y(x,0) + V C_y(x,0)] \quad (3.43)$$

where

$$A_y(x,0) = \left. \frac{\partial A(x,y)}{\partial y} \right|_{y=0} \quad (3.44)$$

$$B_y(x,0) = \left. \frac{\partial B(x,y)}{\partial y} \right|_{y=0} \quad (3.45)$$

and

$$C_y(x,0) = \left. \frac{\partial C(x,y)}{\partial y} \right|_{y=0} \quad (3.46)$$

Integrating over the x dimension gives the total current,  $I_p$ , flowing across the p-i junction per unit depth:

$$I_p = \int_0^a J_p(x,0) dx \quad (3.47)$$

$$I_p = -2qD_p \int_0^a [A_y(x,0) + U B_y(x,0) + V C_y(x,0)] dx \quad (3.48)$$

$$I_p = -2qD_p [A_o + U B_o + V C_o] \quad (3.49)$$

where

$$A_o = \int_0^a A_y(x,0) dx \quad (3.50)$$

$$B_o = \int_0^a B_y(x,0) dx \quad (3.51)$$

and

$$C_o = \int_0^a C_y(x,0) dx \quad (3.52)$$

At  $y=b$ , the n-i junction, we can similarly state

$$J_p(x,b) = 0 \quad (3.53)$$

$$J_n(x,b) = 2qD_n \left. \frac{\partial n(x,y)}{\partial y} \right|_{y=b} \quad (3.54)$$

$$J_n(x,b) = 2qD_n [A_y(x,b) + U B_y(x,b) + V C_y(x,b)] \quad (3.55)$$

Again, integrating over the x variable,

$$I_n = 2qD_n [A_b + U B_b + V C_b] \quad (3.56)$$

where  $A_b$ ,  $B_b$  and  $C_b$  have definitions similar to (3.50) - (3.52).

Since the current through the device must be continuous, the hole current across the p-i junction (3.49) must equal the electron current across the n-i junction (3.56). Equating these two expressions and rearranging terms, a relationship between the boundary densities results, namely,

$$U = - \frac{D_n A_b + D_p A_o}{D_p B_o + D_n B_b} - V \frac{D_n C_b + D_p C_o}{D_p B_o + D_n B_b} \quad (3.57)$$

The previously unspecified boundary conditions,  $U$  and  $V$ , are fixed relative to one another. Although an analytic expression for either of these values has not been determined, an examination of the open circuit conditions does yield such a value for this single operating point. Open circuit conditions dictate that the net junction currents be zero so that  $I_p = 0$  and  $I_n = 0$ . Setting  $I_p$  and  $I_n$  equal to zero, we obtain from Eq. (3.49)

$$A_o + U_o B_o + V_o C_o = 0 \quad (3.58)$$

and from Eq. (3.56)

$$A_b + U_o B_b + V_o C_b = 0 \quad (3.59)$$

The subscript  $o$  attached to  $U$  and  $V$  denote open circuit densities.

Elimination of  $U_o$  in the above two equations results in an expression for the boundary density  $V_o$  given by

$$V_o = \frac{A_o B_b - A_b B_o}{C_b B_o - C_o B_b} \quad (3.60)$$

Knowing the boundary density,  $V_o$ , the remaining boundary density  $U_o$  can be found either by eliminating  $V_o$  from (3.58) and (3.59), or by substituting (3.60) into (3.57). Thus, for open circuit conditions, the optically generated carrier density can be completely described. Also, with the boundary densities known, the junction potentials can be

found from the definitions given in Equations (3.7) and (3.8). In particular,

$$V_p = \frac{kT}{q} \ln \left( \frac{U_o}{n_i} + 1 \right) \quad (3.61)$$

and

$$V_n = \frac{kT}{q} \ln \left( \frac{V_o}{n_i} + 1 \right) \quad (3.62)$$

These junction potentials,  $V_p$  and  $V_n$ , are the potential differences across the p-i and n-i junctions due to the presence of an excess carrier density within the intrinsic region. Hence, these potentials are in excess of the equilibrium junction voltages. The open circuit voltage of the solar cell is a result of these optically induced voltages.

The open circuit voltage can be found by summing the optically induced potentials. The junction potentials have been found above, but the potential drop across the intrinsic region remains to be found. Because of the difference of diffusion coefficients for holes and electrons, the boundary densities are not equal in general. This inequality results in a nonsymmetric carrier distribution across the intrinsic region. Such a distribution gives rise to a voltage drop across the i region. When the cell is loaded and a current is allowed to flow, there is also an ohmic drop across the i region. To assess the magnitude of these voltage drops across the intrinsic region of the solar cell, we must first determine the electric field within this region and

then integrate the field expression from the p to the n junction to obtain the total drop across the active region of the cell. To determine the expression which describes the electric field within the intrinsic region, first consider the sum of the current components at a point (x,y) given by

$$J_T(x,y) = J_p(x,y) + J_n(x,y) \quad (3.63)$$

or

$$J_T(x,y) = q[\mu_n + \mu_p][n(x,y) + n_i] E(x,y) + q[D_n - D_p] \frac{\partial n(x,y)}{\partial y} \quad (3.64)$$

Recall that the total current across the p-i junction is composed of entirely hole current. From Eq. (3.42), we can write

$$J_T(x,y) = J_p(x,0) = -2qD_p \frac{\partial n(x,y)}{\partial y} \Big|_{y=0} \quad (3.65)$$

Combining Equations (3.65) and (3.64), and rearranging terms,

$$E(x,y) = - \frac{2D_p}{\mu_n + \mu_p} \frac{\partial n(x,y)}{\partial y} \Big|_{y=0} \frac{1}{n(x,y) + n_i} - \frac{D_n - D_p}{\mu_p + \mu_n} \frac{1}{n(x,y) + n_i} \frac{\partial n(x,y)}{\partial y} \quad (3.66)$$

Integrating this expression for the field, the voltage drop across the intrinsic region is given by

$$\begin{aligned}
 V_i &= - \int_0^b E(x,y) dy \\
 V_i &= \frac{2D_p}{\mu_n + \mu_p} \left. \frac{\partial n(x,y)}{\partial y} \right|_{y=0} \int_0^b \frac{dy}{n(x,y) + n_i} \\
 &\quad + \frac{D_n - D_p}{\mu_p + \mu_n} \int_0^b \frac{\partial n(x,y)}{\partial y} \frac{dy}{n(x,y) + n_i}
 \end{aligned} \tag{3.67}$$

From Eq. (3.67), we see that the potential drop across the intrinsic region arises from the two effects which have been mentioned above. The ohmic drop arising from current flow through the device is given by the first term on the right hand side of the equation, while the remaining term describes the potential drop due to the carrier gradient across the intrinsic region. The total drop across the intrinsic region as described by Eq. (3.67) is actually a function of the spatial variable  $x$ . Thus, the internal voltage drop at the top of the cell may be different than that at the bottom of the cell. This variation is a result of the carrier concentration gradient between the illuminated side and the dark side of the cell. This is often referred to as the transverse photo voltage, and it is a small effect on the order of millivolts. Hence, the  $x$  variation can be reasonably neglected.

The terminal voltage of the pin solar cell can be calculated using the values obtained from Equations (3.67), (3.61) and (3.62) which yields

$$V_{\text{term}} = V_p + V_n - V_i \quad (3.68)$$

For the open circuit condition, a simplification can be made to Eq. (3.67). Since there is no ohmic drop for this case, only the distribution related term contributes to the lateral voltage drop so that

$$V_{\text{ioc}} = \frac{D_n - D_p}{\mu_n + \mu_p} \int_0^b \frac{\partial n(x,y)}{\partial y} \frac{dy}{n(x,y) + n_i} \quad (3.69)$$

At this point, all the equations necessary for the determination of the current voltage characteristic have been derived. Although a closed form current-voltage equation cannot be written, iterations using the above expressions can generate a current voltage curve for the pin solar cell.

With the aid of a computer, iterative calculations would proceed as follows. To begin, the boundary densities for open circuit conditions can be found from Equations (3.60) and (3.57). These densities specify the junction potentials as defined in Equations (3.61) and (3.62). The voltage drop across the intrinsic region can be calculated from Eq. (3.69), and the terminal open circuit voltage can be obtained from Eq. (3.68). This now gives the first point on the current voltage curve. To obtain the remaining curve, the following process is repeated:

1. Decrease the junction potential,  $V_n$ , by a specified increment and calculate  $V$  using the boundary condition (3.8).
2. Calculate the p boundary condition  $U$  using the expression (3.57). The junction potential can be found for the p-i junction from (3.61).
3. The voltage drop across the intrinsic region can now be found with (3.67).
4. The above three potentials sum to the terminal voltage as described in (3.68).
5. The terminal current can be calculated from Eq. (3.49).

The above sequence arrives at another point on the curve. By repeating this process, the entire characteristic can be found for the pin solar cell. With the aid of the CDC 6400 computer located at The University of Arizona Computer Center, the above procedure was carried out to obtain current voltage curves for several pin solar cell configuration and illumination variations. Results from these computations are presented in Chapter 4.

## CHAPTER 4

### RESULTS

A method of fabricating the pin solar energy converter has been described and details of the testing procedure were outlined in Chapter 2. A model for the solar cell was derived in Chapter 3. The test results of the actual fabricated devices will now be presented and discussed along with the expected results obtained from the computer solution of the model.

#### Experimental Results

Two lots of the solar cell were processed, and each lot contained both the large groove cells and the small groove cells. Processing of the various cell types was identical except for the longer etch time required for the large groove devices. The starting material used in the fabrication of the solar cells was lightly doped p-type silicon of 20 to 40 ohm-cm resistivity.

Completed devices were observed on a curve tracer, and the DC characteristic, I vs. V curve, served as an initial screening of the solar cells. In particular, devices which were shorted, displayed soft or leaky characteristics or exhibited low sensitivity to illumination by a microscope light were not further tested. Additional data was taken under solar illumination on a total of nineteen (19) small groove cells and nineteen (19) large cells from the two lots. Testing was

performed in accordance with the procedure described in Chapter 2.

Example results from these tests are summarized below.

Lot 1, Cell No. 4-E2 Large Grooves

This cell was tested at its original thickness of 10 mil and after successive etch thinning of the wafer. Figures 4.1 and 4.2 show open circuit voltage ( $V_{oc}$ ) and short circuit current ( $I_{sc}$ ) dependence on wafer thickness for this particular cell. The dip in curves is attributed to surface effects resulting from a variation in surface conditions obtained in the etch thinning process. The etch process, which lacked the proper process control, produced these variable results, and not all wafers exhibit the same characteristics. Two extreme surface conditions could give rise to reduced output at the 7 mil thickness. First, a highly reflective surface would result in fewer optically generated electron-hole pairs and a reduced output. The other extreme condition would be a rough, highly damaged surface which is characterized by extremely high surface recombination velocities. Under this condition the electron-hole pairs would be lost to surface recombinations and again a reduced output would be experienced. Curves shown in Figures 4.1 and 4.2 show that both  $V_{oc}$  and  $I_{sc}$  are significantly affected by the surface condition. Theoretical results presented in the next section show that variations in surface recombination velocity does not significantly affect  $I_{sc}$ . Thus, the surface recombination explanation seems unlikely, and surface reflectance appears the probable cause of reduced output.  $V_{oc}$  and  $I_{sc}$  values are poor at best; efficiency for this cell is somewhat

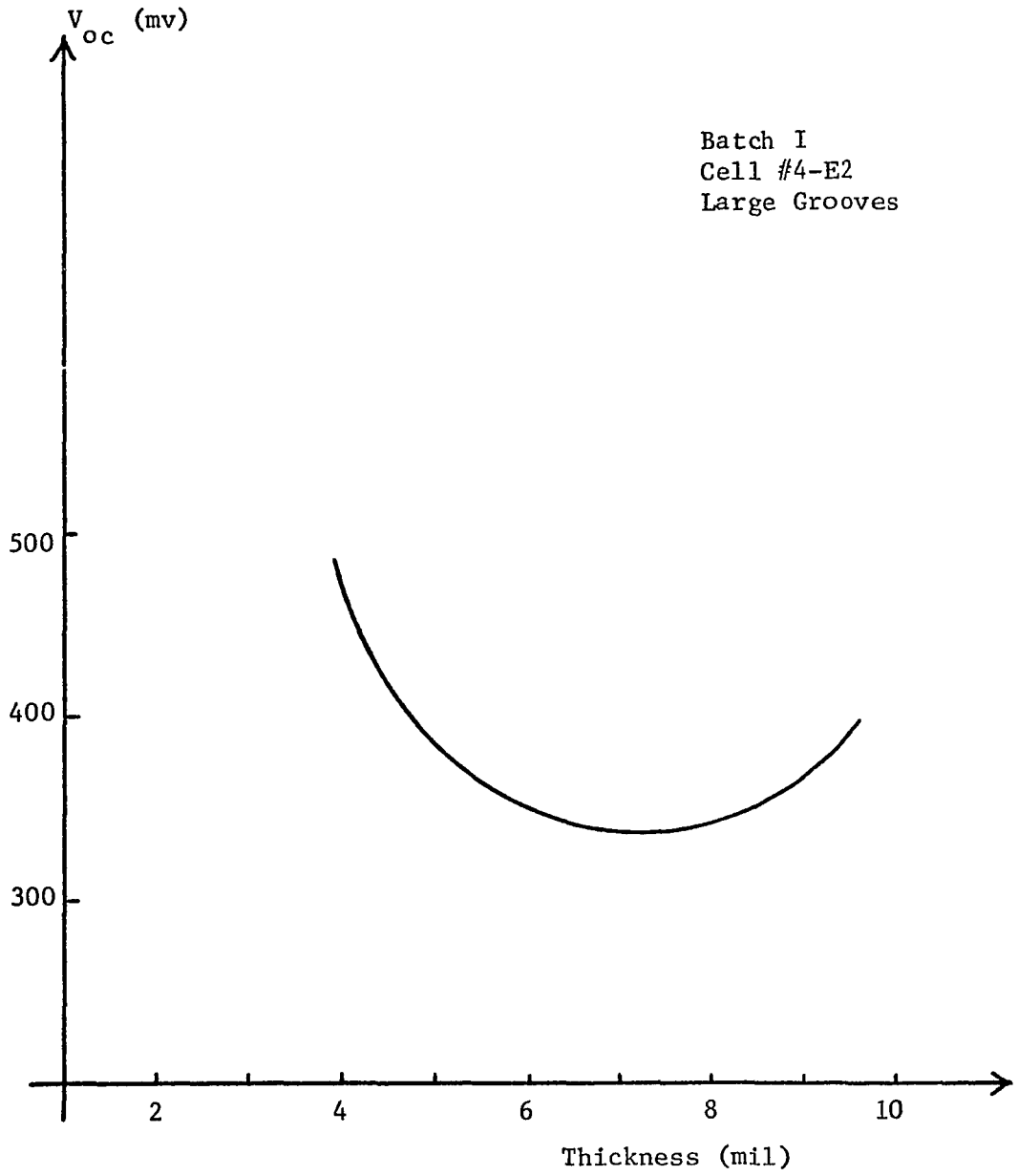


Fig. 4.1  $V_{oc}$  Versus Cell Thickness, Cell #4-E2

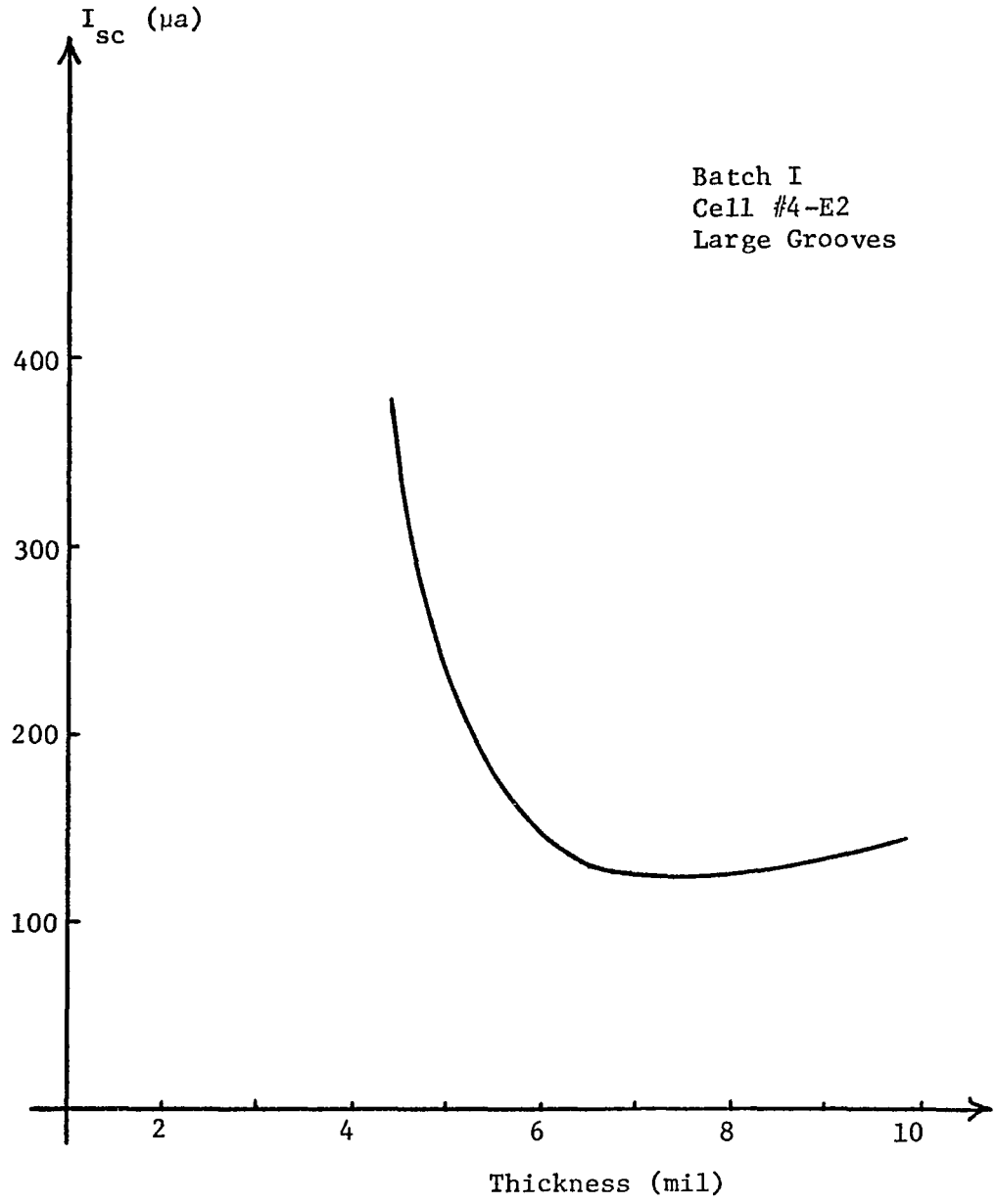


Fig. 4.2  $I_{sc}$  Versus Cell Thickness, Cell #4-E2

less than 2%. This low level of performance is representative of that obtained for all large groove cells.

#### Lot 1, Cell No. 1-A2 Small Grooves

This cell was tested before thinning with an 800 Å thermally grown silicon dioxide coating over the illuminated surface. An open circuit voltage of 240 mv and a short circuit current of 68 µa were obtained for this case. Figures 4.3 and 4.4 show the  $V_{oc}$  and  $I_{sc}$  variations with wafer thickness for both the coated and bare silicon surfaces. The steady increase in  $V_{oc}$  and  $I_{sc}$  with decreasing cell thickness is expected. The carrier generation, as described by Eq. (3.2), is greatest at the illuminated surface. Thus, one would expect the cell output to increase as this surface is brought closer to the collecting junctions. The best voltage current characteristics was obtained for a wafer thickness of 3.0 mil, and the V-I curve for this case is shown in Fig. 4.5. This curve shows a  $V_{oc}$  of 444 mv and a  $I_{sc}$  of 0.99 ma. The curve fill factor, CFF, for this curve was found to be 0.51, and the maximum power output was 0.22 mw. Taking the cell area into account, this corresponds to a maximum power output yield of 7.42%. This was the highest cell efficiency obtained for any of the cells.

#### Lot 2, Cell No. 2-B2 Small Grooves

The  $V_{oc}$  and  $I_{sc}$  variations with wafer thickness were found to be somewhat erratic for this cell, and the observed values are listed in Table 4.1 for both coated and bare silicon wafer surfaces. The erratic behavior is again attributed to surface effects resulting from the etch

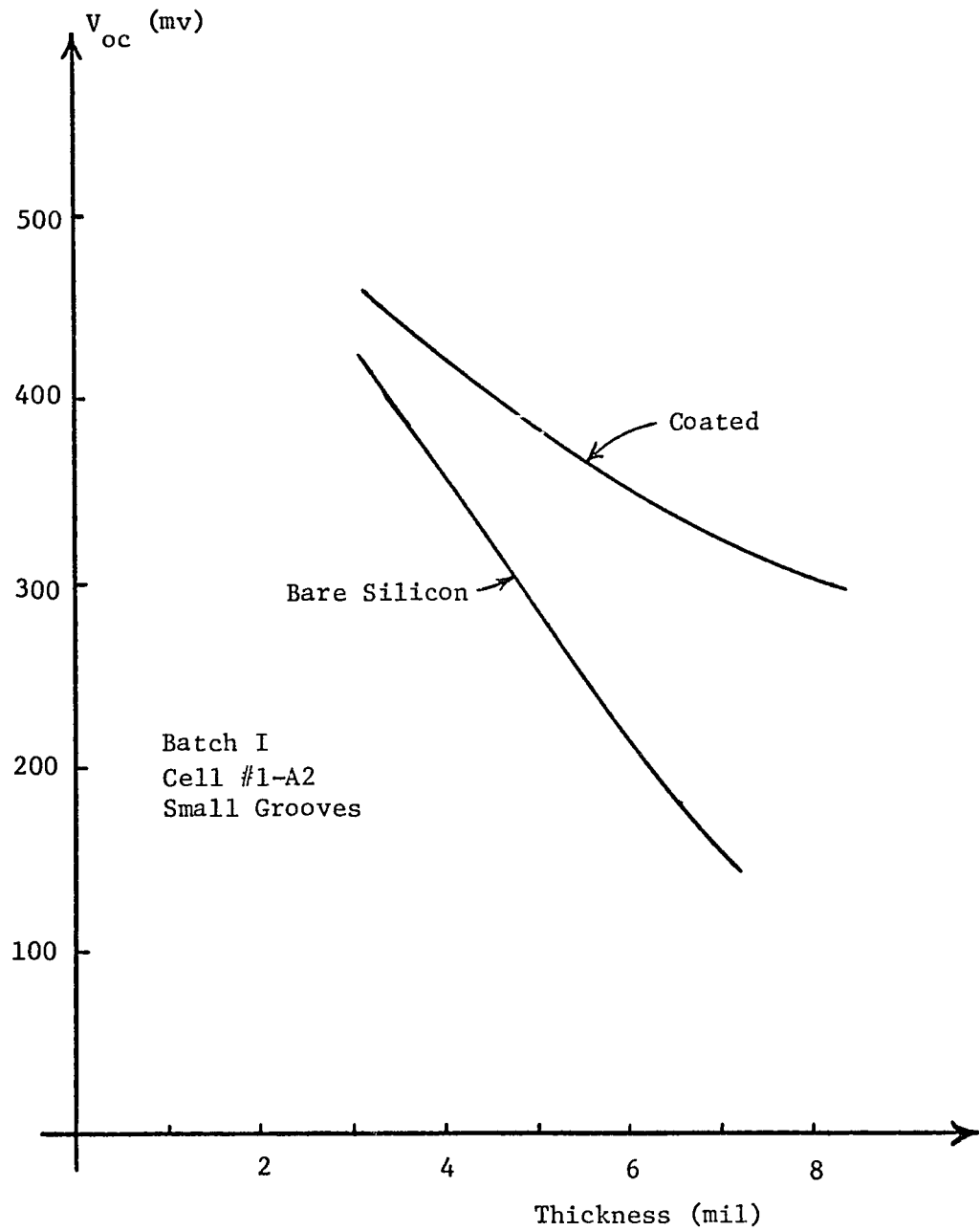


Fig. 4.3  $V_{oc}$  Versus Cell Thickness, Cell #1-A2

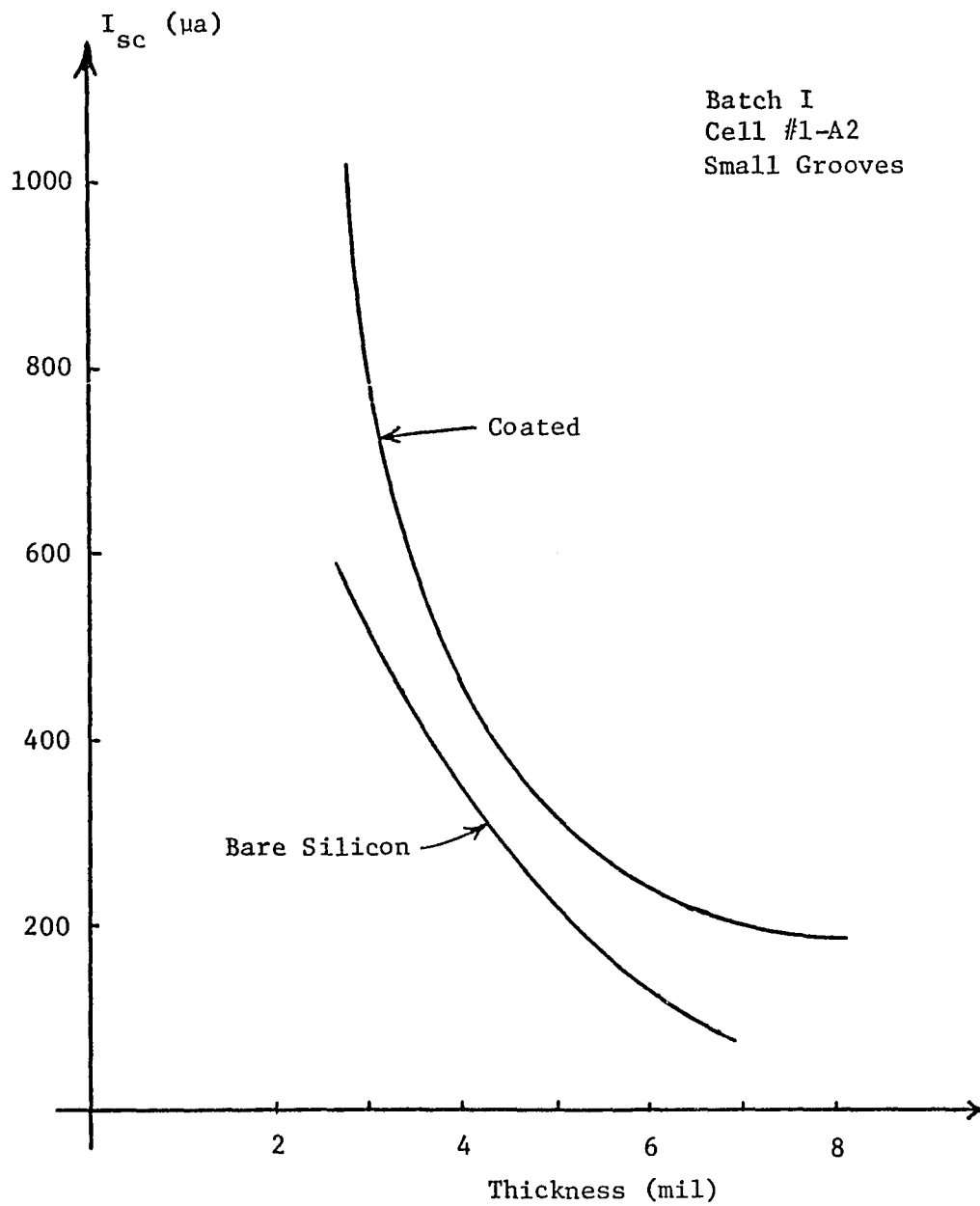


Fig. 4.4  $I_{sc}$  Versus Cell Thickness, Cell #1-A2

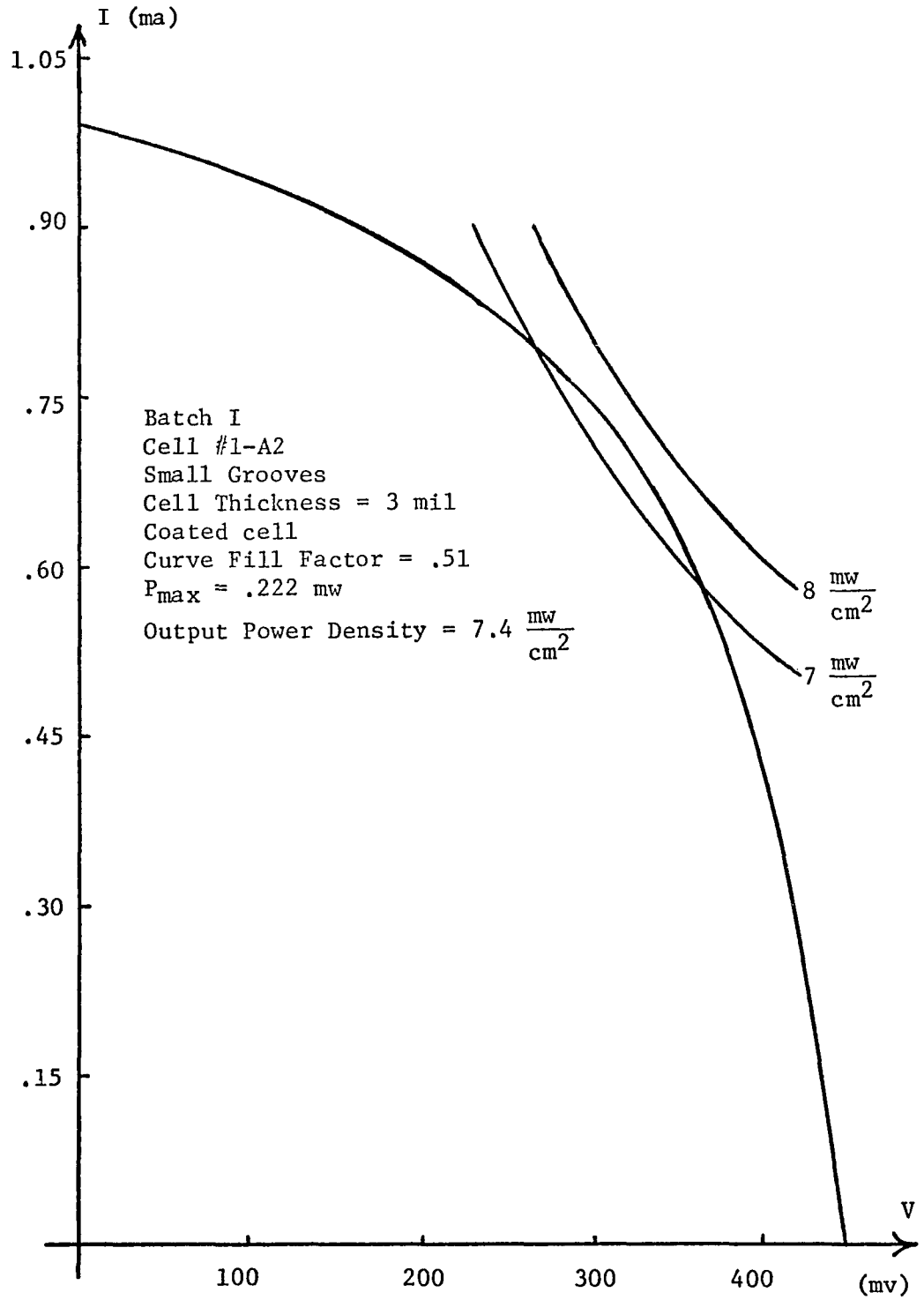


Fig. 4.5 V-I Characteristic of Cell #1-A2

Table 4.1  $V_{oc}$  and  $I_{sc}$  Variation with Thickness

Thickness	$V_{oc}$ (mv)	$I_{sc}$ (ma)	Surface
10.0	390	.390	Bare Si
8.0	360	.078	Bare Si
5.5	350	.390	Bare Si
4.5	430	.660	Bare Si
4.5	390	.870	Coated
3.0	430	.760	Coated

thinning process. The optimum V-I characteristic was found for a wafer thickness of 3 mils, and this curve is shown in Fig. 4.6. The output power density for the cell was found to be  $4.67 \text{ mw cm}^{-2}$ , whereas the solar input to the cell for the day and time it was tested was estimated to be  $86.72 \text{ mw cm}^{-2}$ . This yields a cell efficiency of 5.38%.

#### Discussion of Test Results

The performance of the solar cells fabricated as described in Chapter 2 has exhibited several shortcomings. The most detrimental of these is the low curve fill factor which was 0.51 for the best cell tested. This degradation agrees with findings which were published subsequent to the fabrication period of this investigation. Fischer and Gereth [1971] have found that sintered aluminum contacts degrade the curve fill factor typically to a value of approximately 0.4. They also show that an alternative metallization system, namely titanium-silver, produces contacts which raise the CFF to a value of 0.7. While Fischer and Gereth do not postulate the physical cause of the aluminum contact degradation, a mechanism of silicon dissolution into aluminum at sintering temperatures in excess of  $450^{\circ}\text{C}$  has been reported [McCarthy, 1970]. This silicon dissolution occurs in localized areas and results in deep pits which can extend in excess of  $1 \mu\text{m}$  into the silicon. This reaction is particularly evident in shallow junction devices, such as this solar cell, and results in localized junction shorts.

If a non-dissolution type contact was employed on the solar cell and the CFF could be increased to 0.7, then the efficiency of the best cell (Cell No. 1-A2) would be raised to about 10%. The V-I curves

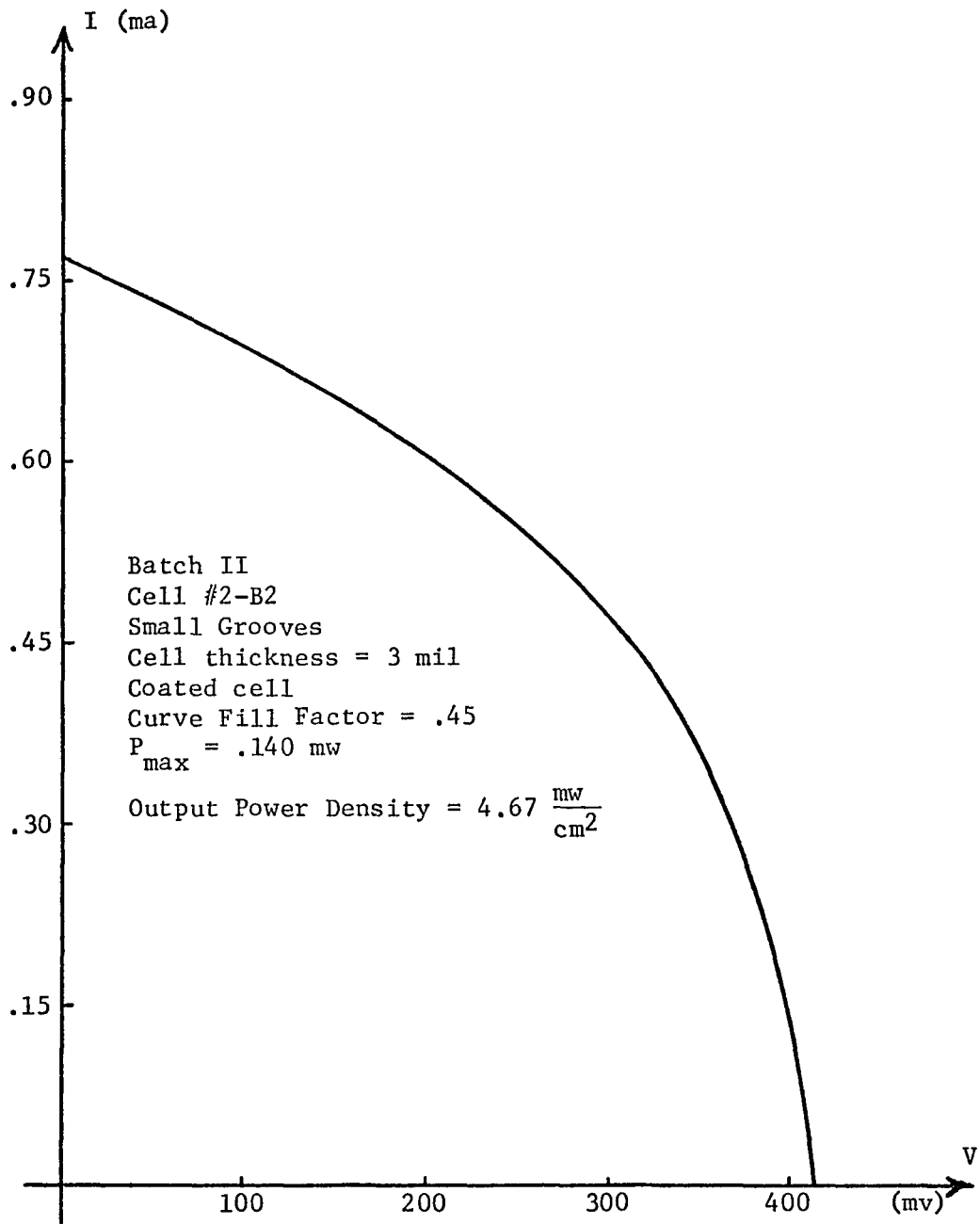


Fig. 4.6 V-I Characteristic of Cell #2-B2

presented by Fischer and Gereth also show that the sintered aluminum contacts reduce the maximum open circuit voltage as well as the CFF. If the percentage degradation in  $V_{OC}$  by aluminum contacts compared to the Ti-Ag contacts is removed, then the 10% efficiency level cited above would be raised to 12.5%. Hence, by employing the proper contact material, the small groove, 3 mil thick, pin solar cell should be capable of achieving this 12.5% level of efficiency.

The performance of the large groove cells was found to be significantly poorer than that of the small groove cells. This is attributed in part to the fact that the optically generated electron-hole pairs have a greater distance to diffuse before being collected, so that more carriers are lost to recombination. However, as will be shown in the next section, the greater separation of the collecting junctions does not account for the greatly reduced output of the large groove cells. Consider, however, the effect of aluminum into the silicon junction which can cause junction shorting. The large groove cells are composed of ten (10) grooves, each 4.5 mils deep, separating nine (9) active generation regions. Compare this to the small groove cells formed by twenty-four (24) grooves of 1.5 mil depth separating twenty-three (23) active generation regions. The large groove cells have a larger aluminum-silicon contact area, larger than the small groove cells by a factor of 1.25. One can then expect a proportionately higher number of junction shorts. For such a short on the large structure which degrades a single generation region, 11.1% of the entire

cell is affected by this degradation. In contrast, for each generation region which is degraded on the small structure, only 4.35% of the cell is affected. As the large groove cells have a larger contact area than the small groove cells, the large grooved structures are also more susceptible to junction shorting or degradation. More importantly, because of the fewer number of generation regions in the large structure, each such junction degradation has a more pronounced overall effect on the entire cell performance. Since the fabrication phase of this study had been completed before the appearance of the Fischer and Gereth paper which alluded to the silicon dissolution mechanism, experiments could not be performed to verify the dissolution effects, but the large groove cell degradation due to these effects is highly probable.

#### Analytical Results

An analytical model which describes the pin solar energy converter was derived in Chapter 3. In addition to the stated assumptions, several implicit assumptions should be noted. Specifically, the model does not account for reflections from the front surface. The density of generated carriers obtained in the analysis should therefore be larger than the density established in the actual cell. The vertical junction geometry used in the analysis results in a larger volume of active generation region which makes the number of generated carriers larger in the theoretical analysis than in the actual cell. Both of the above assumptions tend to increase the cell output. Thus, the results of the analysis tend toward an upper bound on the cell performance.

Also presented with the derivation of the model was an iterative scheme to generate the current-voltage characteristic of the diode. This iterative approach begins by imposing open circuit conditions to obtain the first point on the curve, and succeeding iterations calculate points on the curve until a negative voltage results which indicates a reverse biased diode. As the reverse characteristic of the diode is extremely flat, a terminal voltage within several millivolts of true short circuit conditions yields an accurate short circuit current. Similarly, if one chooses a sufficiently low boundary carrier density, indicative of a reverse biased junction, a single pass through the density and voltage calculations lead directly to the short circuit current. Thus, by imposing the open circuit conditions and assuming a low boundary density, the extreme points of the I-V characteristic can be found with only two sets of calculations. This method of computation had to be employed to characterize the effect of several parameters of the pin solar cell because the complete program execution time was rather long and only a limited amount of computer time was available. By obtaining the open circuit and short circuit parameters, the output power of the cell can be inferred if a constant curve fill factor is assumed for all parameter variations.

Previous mention was made that as the groove spacing is increased, more of the optically generated carriers in the *i* region are lost to recombination. The effect was studied by observing the open circuit voltage and short circuit current as a function of  $L^*/B$ , the ambipolar diffusion length to groove spacing ratio. The results are

shown in Figures 4.7 and 4.8. This evaluation was carried out by holding the surface recombination velocity and spectral input constant. A 200 cm/sec recombination velocity was assumed for the illuminated surface and 500 cm/sec on the dark surface. The spectral input was adjusted to be representative of solar illumination at the earth's surface by weighting the solar spectrum with the optical depth data given by Shaw [1971], and also Shaw, Reagan, and Herman [1973], which yielded  $105 \text{ mw/cm}^2$ . The small arrows appearing on Figures 4.7 and 4.8 indicate a diffusion length of 0.04 cm which is typical for the fabricated pin solar cell. Figure 4.7 shows that the open circuit voltage for the large groove cell is greater than the small groove structure. This is due to a larger carrier concentration generated in the correspondingly larger intrinsic region. The existence of this larger electron-hole pair concentration in the intrinsic region of the larger structure also gives rise to a correspondingly larger short circuit current density. However, the total short circuit current is less for the large groove cells because the total collection length, i.e., metal contact length, is less for the large groove cell.

Figure 4.8 clearly shows the effect of diffusion length on the short circuit current. The flattening of the curves at the larger  $L^*/B$  ratios is indicative of the fewer number of carriers which are lost to bulk recombination. As the diffusion length is defined as the average distance a carrier diffuses before it is lost to recombination, the flat portion of the curve is expected to occur for diffusion lengths several times greater than the groove spacing. The computer data displayed in Fig. 4.8 shows this indeed to be the case. Both figures show that for

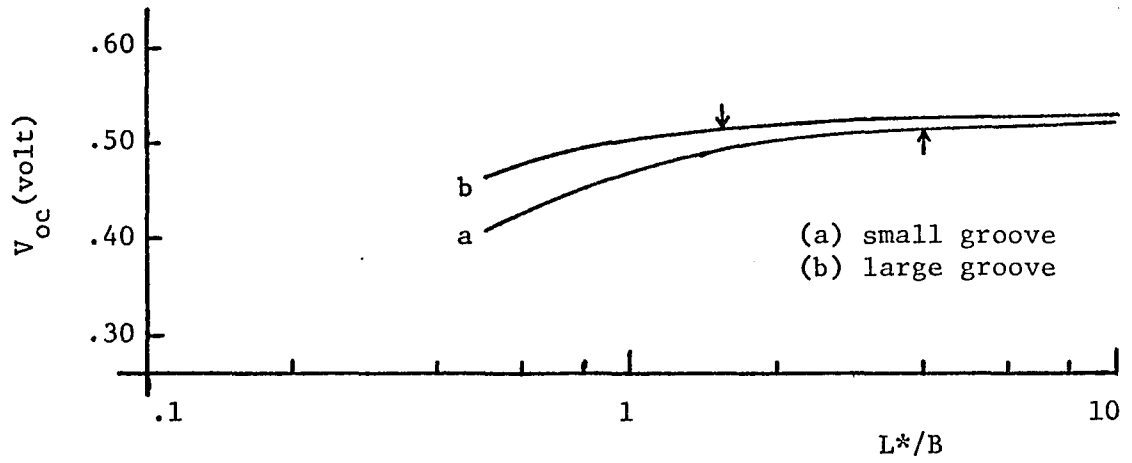


Fig. 4.7  $V_{oc}$  Versus  $L^*/B$

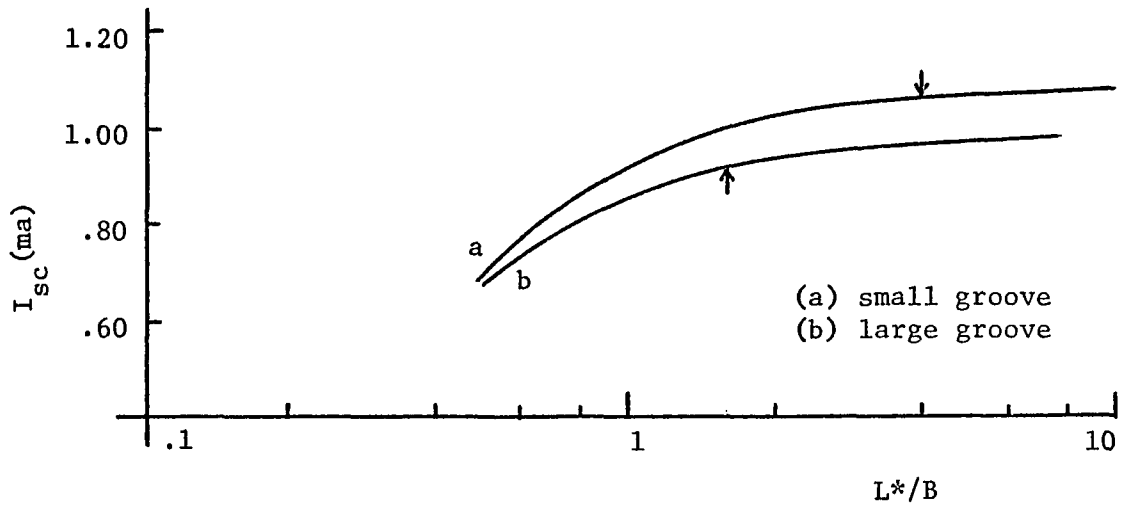


Fig. 4.8  $I_{sc}$  Versus  $L^*/B$

$L^*/B$  ratios larger than three, no significant increases in  $V_{oc}$  or  $I_{sc}$  is obtained. Thus, a design rule for this solar cell is that groove spacing should be maintained at one third of the ambipolar diffusion length or less.

The presence of surface recombination causes the optically generated carrier concentrations to be reduced at the surfaces. The pin solar cell analysis program was written to accept surface recombination velocity as an input parameter for both the illuminated and dark surfaces of the device. Since there are an infinite combination of front and backside recombination velocities, this study was limited to several typical values to evaluate the effect of these parameters on device performance. The backside surface recombination velocity was chosen to be higher than that on the illuminated side as all device processing is carried out on the dark side. Table 4.2 presents the combinations of surface recombination velocities that were considered. The corresponding open circuit voltage and short circuit currents obtained for a pin cell of 3 mil thickness and 3 mil groove spacing with a .04 cm diffusion length are also given in this table.

Results of this evaluation show that the short circuit current is not significantly affected by the variations, but the open circuit voltage is significantly influenced by surface recombination. Examination of the distribution function described by Equations (3.34), (3.35) and (3.36), shows the carrier distributions to be related to surface recombination in a rather complex manner. Referring to the equations used to obtain the junction potentials, (3.61) and (3.62), we see that

Table 4.2  $V_{oc}$  and  $I_{sc}$  Variations with Surface Recombination

Parameter Variation	$V_{oc}$	$I_{sc}$
$S_o = 0$ $S_a = 0$	.62	.88
$S_o = 20$ $S_a = 50$	.59	.89
$S_o = 200$ $S_a = 500$	.52	.84

the boundary densities determine these values. The boundary densities, which are equal for the open circuit case, are given by expression (3.60). The boundary densities,  $U_o$  and  $V_o$ , are determined by the boundary related terms  $A_o$ ,  $A_b$ ,  $B_o$ ,  $B_b$ ,  $C_o$  and  $C_b$ . Additional output from the computer evaluation gives the values of these terms. Using these numerical values in Eq. (3.60), one finds that the numerator of Eq. (3.60) is relatively insensitive to surface recombination variations, but the resulting variations in the denominator are responsible for the variations in the boundary densities.

Chapter 3 presented a derivation for the voltage drop across the intrinsic region of the pin solar cell, and the result was given in expression (3.67). As was pointed out there, the lateral voltage drop is a function of the spatial coordinate  $x$ , the depth into the cell. This variation was cited to be small. The 3 mil thick cell with 3 mil groove spacing was analyzed to verify the magnitude of this  $x$  dependence on the lateral voltage. The points chosen for this evaluation were  $x = 0.1$  and  $0.9$  of the cell thickness. Table 4.3 gives the calculated values of the intrinsic voltage drop,  $V_i$ , at these points under short circuit conditions.

Table 4.3 Lateral Voltage Drop as a Function of Depth

Depth into Cell (mil)	$V_i$ (volts)
.3	.1313
2.7	.1259

As the difference between these points is less than 6 mv, the assumption that this transverse (vertical) voltage is negligible is indeed justified. Examination of computer output shows that the resistive component of the potential drop decreases with depth into the cell while the distribution component increases with the depth into the cell. Since the sum of these individual contributions decreases toward the dark side, the resistive contributions is seen to dominate. Referring to Eq. (3.67), the first term on the right hand side is the resistive component. The form of the generation term, expression 3.2, indicates that the carrier density  $n(x,y)$  decreases with depth into the cell. Thus, the total current flow is expected to decrease and the resistivity is expected to increase as a function of depth. The total current flow is represented by the term

$$\left. \frac{\partial n}{\partial y} \right|_{y=0}$$

and the resistivity is proportional to the integral term. Of these two opposing tendencies the decrease in current flow is the influence factor which results in an overall decrease in the resistive component of the lateral voltage of the cell.

Now let's focus attention on the second term on the right hand side of (3.67), the distribution term of the lateral voltage drop. As explained above,  $n(x,y)$  decreases as a function of depth so that the term

$$1/[n(x,y) + n_i]$$

will cause the distribution term to increase with depth. The density

of generated carriers is expressed as an expansion of sine functions in the y dimension. Thus, the term  $\partial n/\partial y$  within the integral takes on both positive and negative values over the range of integration. The net result is that the integral of the product of the partial derivative and the reciprocal of the density yields an increasing potential as a function of depth into the cell.

All of the computer analysis to this point has been directed at obtaining insight to the effect of material parameters using the open circuit voltage and short circuit current to evaluate the results. These device terminal parameters are related to the maximum output power,  $P_{\max}$ , of the solar cell by the expression

$$P_{\max} = CFF \cdot I_{sc} \cdot V_{oc} \quad (4.1)$$

where CFF is the curve fill factor. The CFF can be inferred from a plot of the I-V characteristics of the pin solar cell. The iterative scheme developed in Chapter 3 was employed to obtain these curves which are shown in Fig. 4.9. The three curves shown represent the characteristics of the pin cell under illumination conditions at the earth's surface, above the atmosphere, and above the atmosphere under the influence of solar concentrators to effectively double the solar input to the cell. For the case of illumination at the earth's surface, the solar spectral distribution was modified by the atmospheric effects as described by the optical depth data referred to in Chapter 2 under testing. Device material parameters used for these runs were  $S_o = 200$  cm/sec,  $S_a = 500$  cm/sec, cell thickness = 3 mil, groove spacing = 4 mils and diffusion

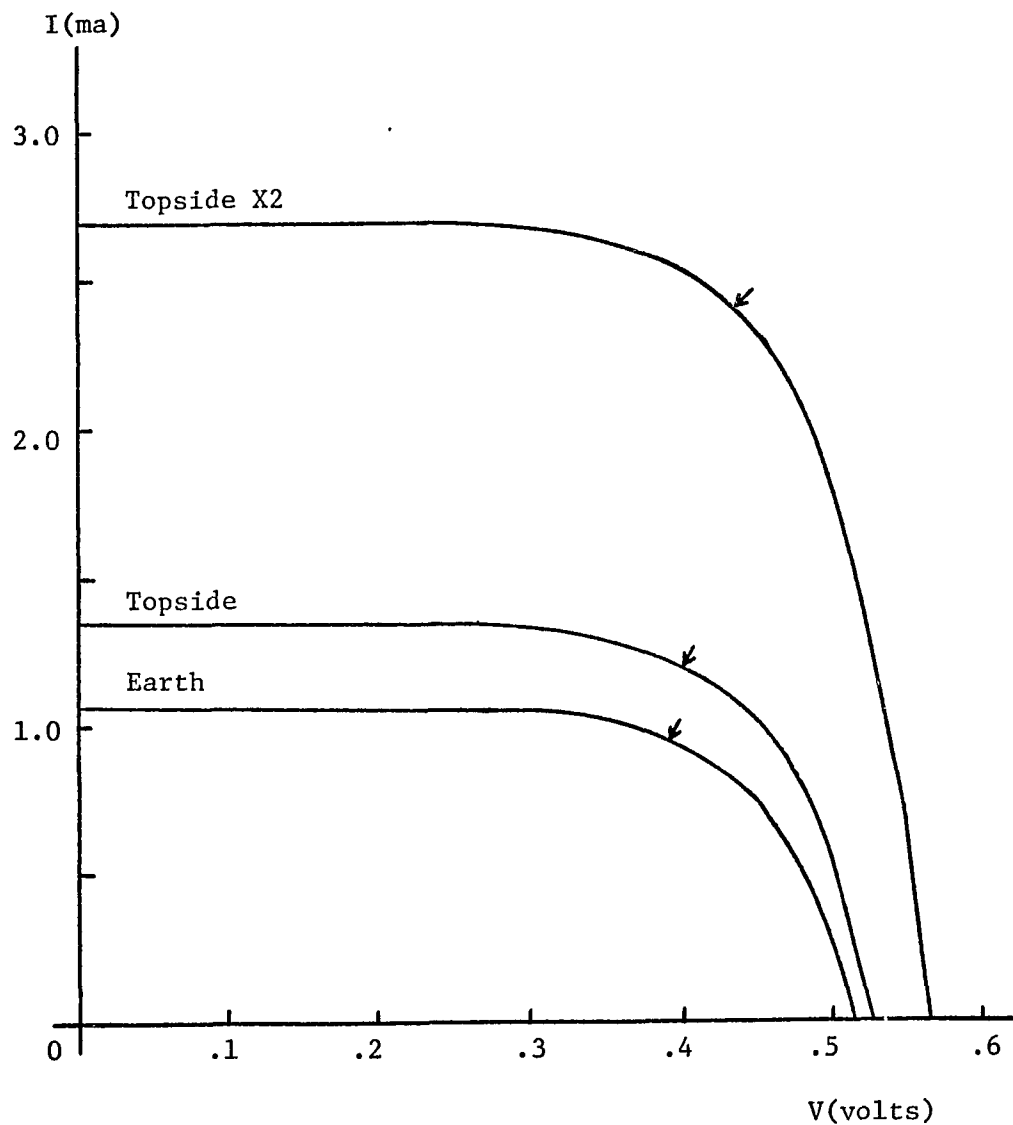


Fig. 4.9 Current Versus Voltage Characteristic from Computer Analysis

length = .04 cm. The small arrows on the curves of Fig. 4.9 indicate the maximum power point,  $P_{\max}$ . The results of this evaluation are summarized in Table 4.4.

The maximum power point,  $P_{\max}$ , curve fill factor, CFF, and the efficiency were calculated from the curve and were not direct output of the computer analysis. The CFF obtained from all three curves is in the range of .67 to .70 which is very close to the expected results as indicated by Fischer and Gereth [1971].

The conversion efficiency shows an interesting tendency. At increasing illumination levels, the overall conversion efficiency increases. Recall from Chapter 3 that the influence of the solar spectrum is reflected only in the A function in the carrier density expression 3.30 and 3.34. A doubling of the solar photon spectral output results in a doubling of the A function. This is also reflected in a doubling in the short circuit current as can be seen in Table 4.4 for the topside and topside X2 results. From (3.57) and (3.60) one can see that the boundary densities also reflect this doubling. However, the resulting junction potentials are related to the natural log of these densities so a lesser increase results. Examination of the expression for the lateral voltage drop across the intrinsic region, (3.67), indicates that for a doubling of the carrier concentration  $n(x,y)$  and a corresponding doubling of the current, which is proportional to

$$\left. \frac{\partial n}{\partial y} \right|_{y=0} ,$$

no increase in the resistive component of the lateral drop is to be

Table 4.4 Summary of I-V Curve Analysis

	Earth	Topside	Topside X2
$V_{oc}$ (volt)	.5156	.5275	.5634
$I_{sc}$ (ma)	1.0746	1.3497	2.6994
$P_{max}$ (mw)	.3730	.4850	1.0500
CFF	.6740	.6820	.6920
% Efficiency	11.7200	11.8200	12.8500

expected. Similarly a doubling of  $n(x,y)$  results in a doubling of  $\partial n/\partial y$ . Hence, the net effect of the doubling is not expected to show any change in the distribution term. The above statements only apply for  $n(x,y)$  large compared to the intrinsic concentration  $n_i$ . Computer output verifies that  $v_i$ , under short circuit conditions, does not change significantly between the topside and topside X2 illumination cases. The terminal voltage for the pin solar cell which is the sum of the junction potentials minus the drop across the intrinsic region directly reflects the individual junction potential increases. The internal voltage drop essentially remains constant for varying illumination conditions. Thus, the increase in conversion efficiency is a result of the increase in boundary densities which are reflected by an increase in junction potentials.

## CHAPTER 5

### CONCLUSIONS

This work has presented a description of the experimental realization and theoretical analysis of a new type of solar cell. A method for the fabrication of this silicon device was discussed, and a mathematical model for the device has been derived. Results obtained for the fabricated devices, including a discussion of the problems encountered in the fabrication, were discussed. Computer solutions of the model were presented which revealed the effects of material parameter variations and device design modifications on the overall performance of the pin solar energy converter.

The results obtained for the fabricated pin solar cell, which yielded a maximum conversion efficiency of 7.3% at the earth's surface, were not encouraging. However, it appears that this conversion efficiency could be raised to over 12% with the development of an improved metal contacting scheme. This conclusion is supported by theoretical analysis of the cell which indicated that a conversion efficiency of 11.7% should be possible at the earth's surface. This efficiency rises slightly to 11.8% above the earth's atmosphere. Another rise in conversion efficiency to 12.8% can be obtained, according to computer solutions, by use of reflectors or lenses to double the solar input to the cell.

Commercially available solar cells which are presently being used on communication satellites typically have a conversion efficiency of

10.5% [Stofel, 1974]. Due to recent advances in the standard vertical collection cells, future satellite solar panels will be assembled using 12% efficient cells. Meanwhile, research and development efforts are producing cells in the 13-14% range; however, difficulties have been encountered in the production of large quantities of this class of cell.

Experimental results described here as well as the theoretical analysis indicates that the pin cell of three mil thickness and four mil groove spacing will convert approximately 12% of the solar input power to electrical power. The dimensions for this cell were dictated by existing processing limitations, and therefore cannot be considered an optimum design configuration. One can conclude that the best cell described here compares favorably with present day solar cells. The fact that this cell is not of optimum design implies that conversion efficiencies above 12% can be achieved with an optimized pin structure.

To advantageously use the enhanced conversion efficiency, solar concentrators must be implemented to increase the illumination level for an energy conversion system. This method is, of course, impracticable for satellite or space application because of weight and volume limitations. However, for application on the earth's surface, where the use of solar concentrators is not restricted, it appears that the pin cell may offer an advantage because of the illumination level dependency of conversion efficiency. It should be noted that the analysis performed here did not consider the effects of cell temperature under the increased illumination level.

Future investigation of the pin solar energy converter should be directed toward the following theoretical and fabrication considerations:

1. Implement an appropriate metallization system to obtain a maximum curve fill factor.
2. Investigate and optimize antireflection coatings for the cell.
3. Develop processing steps which simplify device fabrication. Also, develop a method to fill the grooves to increase the mechanical strength of the cell.
4. Investigate the effects of a lightly doped region as an alternative to the intrinsic region to reduce the ohmic drop within the device, and optimize the cell with respect to resistivity, thickness and groove spacing.
5. Investigate the spatial dependence of the boundary densities,  $U$  and  $V$ , i.e., these quantities were assumed constant for the analysis performed here.
6. Account for the sloping grooves, i.e., extend the analysis to a trapezoidal structure which is more representative of the actual cell.

The suggested fabrication improvements, 1 through 3, can be carried out independent of the remaining theoretical considerations. Of these fabrication improvements, only No. 3 is unique to this new structure cell, whereas the other two are already in common use in the solar cell industry. Suggestion No. 4 may be approached using the analytical

methods described in this paper, while the last two considerations would involve changing the boundary conditions used in deriving the electron-hole carrier distribution. The device analysis can still be used for the new carrier distribution.

## LIST OF REFERENCES

- Chapin, D. M., C. S. Fuller, and G. L. Pearson. "A New Silicon p-n Junction Photocell for Converting Solar Radiation into Electrical Power," Journal of Applied Physics, Vol. 25, p. 676, 1954.
- Finne, R. M., and D. L. Klein. "A Water Amine Complexing Agent System for Etching Silicon," Journal of the Electrochemical Society, Vol. 114, p. 965, 1967.
- Fischer, H., and R. Gereth. "Electrochemically Passivated Contacts for Silicon Solar Cells," IEEE Transactions on Electron Devices, Vol. ED-18, p. 459, 1971.
- Johnson, C. C. "Investigations of Photo Effects in pin Semiconductor Junctions," M.S. Thesis, The University of Arizona, Department of Electrical Engineering, Tucson, Arizona, 1970.
- Kim, C. W., and R. J. Schwartz. "A p-i-n Thermo-Photovoltaic Diode," IEEE Transactions on Electron Devices, Vol. ED-16, p. 657, 1969.
- Kleinman, D. A. "Considerations on the Solar Cell," The Bell System Technical Journal, p. 85, January, 1961.
- McCarthy, J. "Failure of Aluminum Contacts to Silicon in Shallow Diffused Transistors," Microelectronics and Reliability, Pergamon Press, Vol. 9, pp. 187-188, 1970.
- Prince, M. B. "Silicon Solar Energy Converters," Journal of Applied Physics, Vol. 26, p. 534, 1955.
- Shaw, G. E. "An Experimental Study of Atmospheric Turbidity Using Radiometric Techniques," Ph.D. Dissertation, The University of Arizona, Electrical Engineering Department, Tucson, Arizona, 1971.
- Shaw, G. E., J. A. Reagan, and B. M. Herman. "Investigations of Atmospheric Extinction Using Direct Solar Radiation Measurements Made with a Multiple Wavelength Radiometer," Journal of Applied Meteorology, Vol. 12, p. 374, 1973.
- Stofel, E. Hughes Aircraft Co., El Segundo, Ca., Private Communication, May, 1974.

Thekaekara, M. P. "The Solar Constant and the Solar Spectrum Measured from a Research Aircraft," NASA Technical Report TR-R-351, N70-42638, Goddard Space Flight Center, Greenbelt, Md., 1970.

Wolf, M. "Limitations and Possibilities for Improvement of Photovoltaic Solar Energy Converters," Proceedings of the IRE, Vol. 48, p. 1246, 1960.